Available online at www.sciencedirect.com
SCIENCE DIRECT®
Comput. Methods Appl. Mech. Engrg. 193 (2004) 1035–1063
Computer methods in applied mechanics and engineering
www.elsevier.com/locate/cma

Stable particle methods based on Lagrangian kernels

T. Rabczuk, T. Belytschko *, S.P. Xiao

Department of Mechanical Engineering, Northwestern University, 2145 Sheridan Road, Evanston, IL 60208-311, USA

Received 26 March 2003; received in revised form 20 September 2003; accepted 2 December 2003

Abstract

A large deformation particle method based on the Krongauz–Belytschko corrected-gradient meshfree method with Lagrangian kernels is developed. In this form, the gradient is corrected by a linear transformation so that linear completeness is satisfied. For the test functions, Shepard functions are used; this guarantees that the patch test is met. Lagrangian kernels are introduced to eliminate spurious distortions of the domain of material stability. A mass allocation scheme is developed that captures correct reflection of waves without any explicit application of traction boundary conditions. In addition, the Lagrangian kernel versions of various forms of smooth particle methods (SPH), including the standard forms and the Randles–Libersky modification are presented and studied. Results are obtained for a variety of problems that compare this method to standard forms of SPH, the Randles–Libersky correction and large deformation versions of the element-free Galerkin method.

Keywords: Meshfree methods; Particle methods; EFG; SPH

1. Introduction

Meshfree particle methods provide many advantages for modelling severe deformations and failure of solids as compared to Lagrangian finite element and finite difference methods. Although most meshfree methods are basically Lagrangian in character, the absence of a mesh enables them to deal with larger local distortion than finite element methods. Furthermore, phenomena such as fracture and other material instabilities are more easily modelled than with finite elements, particularly when they are not aligned with the nodes.

Particle methods can be classified into those based on kernel approximations, as smooth particle hydrodynamics (SPH) methods, and those based on field approximations, as the element-free Galerkin method (EFG). One of the first meshfree methods was the SPH-method introduced by Lucy [32] and Gingold and Monaghan [20]. It was first utilized for gas dynamic problems. The method was extended to solid continua by Libersky et al. [28], who applied SPH to dynamic fracture and fragmentation of solids,

* Corresponding author. Tel.: +1-847-491-4029; fax: +1-847-491-4011.
E-mail addresses: t-belytschko@northwestern.edu, t-edbelytschko@northwestern.edu (T. Belytschko).

0045-7825/$ - see front matter © 2004 Elsevier B.V. All rights reserved.
doi:10.1016/j.cma.2003.12.005

where mesh-based methods have had difficulties. Fracture was modelled by letting the stresses go to zero after a critical strain.

However, SPH suffers from some inherent difficulties: a lack of consistency that can lead to poor accuracy and a tensile instability that results from the combination of an Eulerian kernel with a Lagrangian description of motion. The latter is more generally a manifestation of the distortion of the domain of material stability, see Belytschko et al. [6,7,47].

In the last 10 years, many improvements have been made in particle methods. Liu et al. [29,30] proposed a correction function that restores linear (first-order) completeness of the kernel function. First-order completeness appears to be a necessary condition for convergence. Furthermore, zeroth-order completeness guarantees global conservation of linear momentum while first-order completeness guarantees global balance of angular momentum as shown in Krongauz and Belytschko [27] and Belytschko et al. [2]. Belytschko et al. [4] showed that these correction methods yield approximations that are identical to the moving least square (MLS) approximation used in EFG [5]. The particle methods based on MLS (or corrected functions), unlike SPH, do not satisfy local conservation of momentum or angular momentum. Dilts [15–17] developed SPH methods based on MLS approximations and extensively studied the issue of local conservation properties.

Johnson and Beissel [24] proposed a modification of the extensional strains of the SPH shape functions, so that they would give the correct values of the extensional strains for linear fields. Subsequently, Randles and Libersky [41] proposed a more general transformation of the gradient that gives the correct values of all strains for linear fields, which they called normalization. Krongauz and Belytschko [27] developed a similar transformation but showed that a standard Bubnov–Galerkin discretization then failed the patch test. Since the patch test is apparently necessary for convergence, this may be quite detrimental to the method. They showed that a Petrov–Galerkin method employing the Shepard functions as test functions and a kernel with a corrected gradient as trial functions meets the patch test. The failure of corrected gradient methods to meet the patch test was subsequently noted by Bonet et al. [13] who proposed solving a subsidiary set of equations to enforce them.

As shown by Swegle et al. [45], particle methods suffer from tensile instabilities. To stabilize SPH, Dyka et al. [18,19] introduced stress points into SPH. This approach was later extended to higher dimensions by Randles et al. [42]. It was shown in [6] that the stress point technique stabilizes SPH by suppressing spurious singular modes observed in SPH, but it does not eliminate the distortion of the domain of material instability. Chen et al. [14] have developed an integration technique based on contour integrals that avoids volumetric locking and appears to eliminate spurious singular modes.

In most of the SPH literature an Eulerian kernel is taken as the weighting function. Recently, Belytschko et al. [6,7] investigated Eulerian and Lagrangian kernels. They pointed out that SPH with stress points and an Eulerian kernel cannot eliminate the tensile instability, because Eulerian kernels distort the domain of material instability; they showed that stress points only remove the instability that arises due to rank deficiency, i.e. spurious singular modes. They also showed that the tensile instability can be avoided by a Lagrangian kernel. However this limits the magnitude of the distortions that can be treated.

Other meshfree methods are the EFG method which uses the MLS approximation [5]. The main contribution of the EFG was the development of methods for treating arbitrary discontinuities, see Belytschko et al. [5,8,9]. It was also used for modeling nonlinear material response under dynamic loading, see [9]. Unlike SPH, the EFG method is discretized by a Galerkin method. The integrals are usually evaluated over background cells based on an octree structure, see [5]. For dynamic applications, cell integration becomes computationally expensive. Beissel and Belytschko [1] developed a nodal integration for EFG, which corresponds to a particle method based on MLS.

In this paper, a meshfree particle method for large deformation, nonlinear problems that employs a Lagrangian kernel with correction of the derivatives, as in Krongauz and Belytschko [27], is described. Stress points are used to eliminate the rank deficiency. It is also shown that through an appropriate con-

struction of the mass matrix, the method accurately treats traction-free boundaries and boundaries with applied tractions, without any special boundary treatment. The method is, however, limited in the amount of deformation it can handle; it is not suitable for problems of fluid flow. Nevertheless, it appears to be able to treat many problems of interest in the simulation of solids, where the deformations of interest are less severe than in fluids. Furthermore, it is stable and robust for this class of problems.

This article is arranged as follows. First, the governing equations are given. After some remarks about Eulerian and Lagrangian kernels, several meshfree approximations are summarized: the original SPH method, the Randles–Libersky [41] correction of the derivatives, the Krongauz–Belytschko correction [27] and the MLS approximation. The discrete governing equations are obtained by collocation as in SPH and by Petrov–Galerkin and Bubnov–Galerkin procedures, respectively. In Section 5, nodal integration, nodal integration with stress points and cell integration used in EFG are reviewed. Then, applications to concrete and metals under quasistatic and dynamic loading are given and compared with experimental data.

2. Governing equations

The governing equations for large deformation problems will first be presented in the total Lagrangian formulation, where the conservation equations and constitutive equations are expressed in terms of the material coordinates $\mathbf{X}$. They will then be presented in the updated Lagrangian formulation, where the equations are described in the current configuration, see Belytschko et al. [10]. We will give both forms of many of the equations.

2.1. Total Lagrangian formulation

We consider a body Ω in $\Re^n$ ($n = 2$ or 3) with boundary Γ; their images in the initial state are Ω_0 and Γ_0, respectively. The initial state will also serve as the reference state. The motion is described by

$$\mathbf{x} = \boldsymbol{\phi}(\mathbf{X}, t), \tag{1}$$

where $\mathbf{x}$ are the spatial (Eulerian) coordinates and $\mathbf{X}$ the material (Lagrangian) coordinates. The displacement is then given by

$$\mathbf{u}(\mathbf{X}, t) = \mathbf{x} - \mathbf{X} = \boldsymbol{\phi}(\mathbf{X}, t) - \mathbf{X}. \tag{2}$$

Neglecting thermomechanical and frictional forces, the conservation equations in the total Lagrangian formulation are given by [10]

$$\varrho J = \varrho_0 J_0, \quad \ddot{\mathbf{u}} = \frac{1}{\varrho_0} \nabla_0 \cdot \mathbf{P} + \mathbf{b}, \quad \dot{e} = \frac{1}{\varrho_0} \dot{\mathbf{F}} : \mathbf{P}^{\mathbf{T}}, \tag{3}$$

where J and J_0 are the Jacobian determinant and initial Jacobian determinant, respectively, $\mathbf{u}$ is the displacement vector, ϱ is the current density, ϱ_0 is the initial density, $\mathbf{P}$ are the nominal stresses (note $\mathbf{P}$ is the transpose of the first Piola Kirchhoff stress tensor as discussed in Belytschko et al. [10]), $\mathbf{b}$ are the body forces per mass unit, e is the internal energy, ∇_0 is the gradient or divergence operator expressed in material derivatives and $\mathbf{F}$ denotes the deformation gradient. Note that the mass conservation equation is written in algebraic form since it is integrable for a Lagrangian description.

The boundary conditions are:

$$\mathbf{u}(\mathbf{X}, t) = \bar{\mathbf{u}}(\mathbf{X}, t) \quad \text{on } \Gamma_0^{\mathrm{u}}, \tag{4}$$

$$\mathbf{n}^0 \cdot \mathbf{P}(\mathbf{X}, t) = \bar{\mathbf{t}}(\mathbf{X}, t) \quad \text{on } \Gamma_0^{\mathrm{t}}, \tag{5}$$

where $\bar{\mathbf{u}}$ and $\bar{\mathbf{t}}$ are the prescribed displacement and traction, respectively, $\mathbf{n}^0$ is the outward normal to the domain and $\Gamma_0^{\mathrm{u}} \cup \Gamma_0^{\mathrm{t}} = \Gamma_0$, $\Gamma_0^{\mathrm{u}} \cap \Gamma_0^{\mathrm{t}} = 0$.

2.2. Updated Lagrangian formulation

In the updated Lagrangian formulation the equations are expressed in the current domain of the body. It should be understood that the governing equations in the total and updated Lagrangian formulation are identical, they are only different descriptions (or transformations) of the same equations.

Neglecting thermomechanical and frictional forces, the conservation equations in the strong form are

$$\dot{\varrho} = -\varrho \nabla \cdot \mathbf{v}, \quad \dot{\mathbf{v}} = \frac{1}{\varrho} \nabla \cdot \boldsymbol{\sigma} + \mathbf{b}, \quad \dot{e} = \frac{\boldsymbol{\sigma}}{\varrho} : \nabla \otimes \mathbf{v}, \tag{6}$$

where $\mathbf{v}$ is the velocity vector, $\boldsymbol{\sigma}$ is the Cauchy stress tensor, e is the internal specific energy and the ∇ is the gradient or divergence operator expressed in spatial coordinates. The energy conservation equation is only necessary as a PDE if heat transfer is relevant. The continuity equation can also be in the form (3a) for an updated Lagrangian description [10]. The boundary conditions are:

$$\mathbf{v}(\mathbf{X}, t) = \bar{\mathbf{v}}(\mathbf{X}, t) \quad \text{on } \Gamma_v, \tag{7}$$

$$\mathbf{n} \cdot \boldsymbol{\sigma}(\mathbf{X}, t) = \bar{\mathbf{t}}(\mathbf{X}, t) \quad \text{on } \Gamma_t, \tag{8}$$

where $\bar{\mathbf{v}}$ and $\bar{\mathbf{t}}$ are the prescribed velocity and traction, respectively, $\mathbf{n}$ is the outward normal to the domain and $\Gamma_v \cup \Gamma_t = \Gamma$, $\Gamma_v \cap \Gamma_t = 0$.

In the updated Lagrangian formulation the constitutive equations are commonly formulated in rate form for large deformations:

$$\boldsymbol{\sigma}^{\nabla} = \dot{\boldsymbol{\sigma}}(\mathbf{D}, q), \tag{9}$$

where q are internal state variables which depend on the material behavior, $\mathbf{D}$ is the rate of deformation or velocity strain and $\boldsymbol{\sigma}^{\nabla}$ is a frame invariant rate. The velocity strain is the symmetric part of the velocity gradient $\mathbf{L}$:

$$\mathbf{D} = \tfrac{1}{2}(\nabla \otimes \dot{\mathbf{x}} + \dot{\mathbf{x}} \otimes \nabla). \tag{10}$$

The antisymmetric part of $\mathbf{L}$

$$\mathbf{W} = \tfrac{1}{2}(\nabla \otimes \dot{\mathbf{x}} - \dot{\mathbf{x}} \otimes \nabla) \tag{11}$$

is the spin-tensor and is needed to calculate certain frame-indifferent rates.

3. Meshfree approximations

Meshfree approximations for a scalar function u in terms of the material (Lagrangian) coordinates can be written as

$$u(\mathbf{X}, t) = \sum_{J \in S} \Phi_J(\mathbf{X}) u_J(t), \tag{12}$$

where $\Phi_J(\mathbf{X})$ are the shape functions and u_J is the value at the particle parameter (it is nearly equal to the displacement) at the position $\mathbf{X}_J$ and S is the set of particles J for which $\Phi_I(\mathbf{X}_J) \neq 0$. Note, that the above form is identical to the form of an FEM approximation. However, in contrast to FEM, $\Phi_I(\mathbf{X})$ is only an approximant and not an interpolant, since $u(\mathbf{X}_I) \neq u_I$. Therefore special techniques are needed to treat displacement boundary conditions, see e.g. [2,17].

The approximation can also be formulated in terms of the spatial (Eulerian) coordinates. In that case, it is conventional to approximate the velocities, instead of the displacements, so

$$\dot{u}(\mathbf{x},t) = \sum_{J\in S} \Phi_J(\mathbf{x})\dot{u}_J(t). \tag{13}$$

Eqs. (12) and (13) correspond to Lagrangian and Eulerian descriptions of motion, respectively. Note, that (13) does not correspond to the standard description of motion for a solid as given in (1). Furthermore, if all dependent variables such as the stress, strain and state variables are expressed in terms of the spatial coordinates $\mathbf{x}$ and time t, then transport terms must be included in the update equations. The shape functions $\Phi_J(\mathbf{X})$ or $\Phi_J(\mathbf{x})$ are obtained from the kernel functions, which are denoted by $W_J(\mathbf{X})$ or $W_J(\mathbf{x})$ for Lagrangian and Eulerian kernels, respectively. Usually radial kernel functions are chosen. For Lagrangian radial kernels $W_J(\mathbf{X}) = W(r_0)$ where $r_0 = \|\mathbf{X} - \mathbf{X}_J\|$ while for Eulerian kernels $W_J(\mathbf{x},t) = W(r)$ where $r = \|\mathbf{x} - \mathbf{x}_J(t)\|$. As noted later, the time dependence of Eulerian kernels is always neglected, see Monaghan [33,34].

The kernel functions are chosen to have compact support. A widely used kernel which has been employed in our calculations is the cubic spline [14]:

$$W(r) = \begin{cases} \dfrac{C}{h^D}(1 - 1.5z^2 + 0.75z^3) & 0 \leqslant z < 1, \\ \dfrac{C}{4h^D}(2-z)^3 & 1 \leqslant z \leqslant 2, \\ 0 & z > 2, \end{cases} \tag{14}$$

where D is the dimension of the space, h is the interpolation radius or radius of the support, $z = r/h$, and C is a constant depending on the dimension

$$C = \begin{cases} 2/3 & \text{for } D = 1, \\ 10/(7\pi) & \text{for } D = 2, \\ 1/\pi & \text{for } D = 3. \end{cases} \tag{15}$$

The support of the kernel function is also called the domain of influence since it determines which neighboring particles effect a given particle and corresponds to S. The relationship of the kernel function to the shape function depends on the approximation technique and is explained in the Sections 3.2–3.5.

3.1. Eulerian and Lagrangian kernels

In most SPH procedures [15–17,41,42] the shape function is directly expressed in terms of an Eulerian kernel:

$$W_J(\mathbf{x}) = W(\mathbf{x} - \mathbf{x}_J(t), h(\mathbf{x},t)). \tag{16}$$

Note that the Eulerian kernel is expressed in terms of spatial coordinates. The radius h of the support can depend on the spatial coordinates.

Belytschko et al. [6] have shown that particle discretizations of solids with an Eulerian kernel with or without stress points lead to a distortion of the stable domain of the material in stress space; the tensile instability analyzed in Swegle et al. [46] is one manifestation of this distortion.

The Lagrangian kernel is expressed in terms of material coordinates, so:

$$W_J(\mathbf{X}) = W(\mathbf{X} - \mathbf{X}_J, h_0). \tag{17}$$

For Lagrangian kernels, the neighbors of influence do not change during the course of the simulation, but the domain of influence in the current configuration changes with time. For radial kernel functions, the

domain of influence in the initial configuration is a circle in two dimensions and a sphere in three dimensions.

The Lagrangian kernel eliminates the tensile instability, but the instability due to a rank deficiency of the discrete equations remains unless stress points are added. Therefore, the representation of the kernel in terms of material coordinates provides a more consistent procedure when simulating material fracture or other material instabilities because instabilities will not occur due to numerical artifacts.

The distortion of material instability is illustrated for the case of a particular material in Fig. 1 [47], which shows the domains of material stability for the Lagrangian kernel, an Eulerian kernel and that of the governing partial differential equation, i.e. the momentum equation (3) for a particular hyperelastic material. The stable domains are shown in the space of the two principal stretches, λ_1 and λ_2. The hyperelastic material model is given by [25]:

$$\boldsymbol{\sigma} = \frac{1}{\sqrt{I_3}}\left[(c_1 + c_2 I_1)\mathbf{B} - c_2\mathbf{B}^2 - \left(c_1 I_3^{\frac{1}{3}} + 2c_2 I_3^{\frac{2}{3}} - \lambda \ln I_3\right)\mathbf{I}\right], \tag{18}$$

where $\mathbf{B} = \mathbf{F}\mathbf{F}^{\mathrm{T}}$. The material constants are $c_1 = 1.265\text{e}5$ N/m^2, $c_2 = 1.012\text{e}4$ N/m^2 and $\lambda = 1.012\text{e}7$ N/m^2. $I_1 = \mathrm{tr}(\mathbf{B})$ and $I_3 = \det(\mathbf{B})$. The material density is $\rho = 125.4$ kg/m^3. In an ideal discretization, the stable domains of the discretization and the PDE should coincide, which is almost the case for the Lagrangian kernel (in fact, the two domains are almost indistinguishable in the figure, but differ numerically). However, for the Eulerian kernel we can see a substantial domain (indicated by grayscale in Fig. 1) where the material should be stable but the discrete model is not. In other words, the shaded area are states of deformation for which the Eulerian kernel is unstable whereas the PDE indicates a stable response.

In the current configuration the domain of influence of a Lagrangian kernel can be extremely distorted. This is a disadvantage in simulating fluid flow problems and other problems with very large distortions. In the following sections the approximation techniques are described in terms of a Lagrangian kernel. The equations for an Eulerian kernel can be derived similarly.

3.2. The SPH approximation

In the SPH method with a Lagrangian kernel, the shape functions are given by a product of the particle volume and the weighting function:

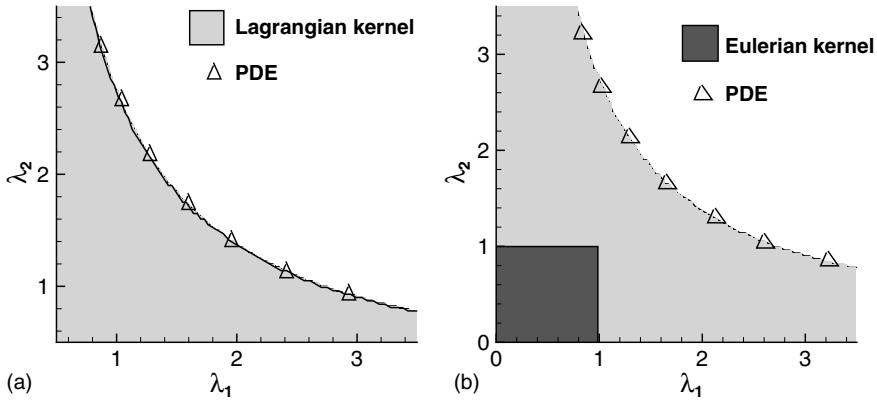

Fig. 1. (a) Stable domain for MLS particle method with stress point integration and Lagrangian kernel compared to the stable domain for the PDE; (b) Stable domains of MLS particle methods for stress point integration with Eulerian and Lagrangian kernel for hyperelastic material; dashed and solid lines bound the stable domains for Lagrangian and Eulerian kernels, respectively.

$$\Phi_J(\mathbf{X}) = W(\mathbf{X} - \mathbf{X}_J, h_0)V_J^0, \tag{19}$$

where V_J^0 is the volume associated with the particle J in the initial configuration. For an Eulerian kernel the shape functions are

$$\Phi_J(\mathbf{x}) = W(\mathbf{x} - \mathbf{x}_J, h)V_J, \tag{20}$$

where V_J is the current volume associated with particle J.

In the application to PDEs, an approximation of a function gradient is needed. In SPH, an approximation of the gradient of a function in terms of the Lagrangian kernel is given by

$$\nabla u^h = -\sum_{J\in S} u_J \nabla_0 \Phi_J \quad \text{with } \nabla_0 \Phi_J = \nabla_0 W(\mathbf{X} - \mathbf{X}_J, h_0)V_J^0, \tag{21}$$

where the ∇_0 indicates the gradient in terms of the material coordinates. The minus sign on the right-hand side of Eq. (21) results from the integration by parts, that is standard in SPH [33,34].

One drawback of the standard SPH-method is its inability to accurately approximate a function when particles are unevenly spaced. This is evidenced by its inability to reproduce linear fields (called the reproducing conditions), which is generally necessary for convergence. The momentum equations with stress rates depending on the velocity gradient are second-order PDEs, so linear completeness, i.e. the ability to reproduce linear functions, is necessary for convergence. These are among the properties checked by the well known patch test. For boundary particles, the constant reproducing conditions are violated even for uniformly spaced particles.

The reproducing conditions (or completeness) of an approximation correspond to the order of the polynomial which can be represented exactly. The following are the conditions for zeroth- and first-order completeness in $\Re^3$:

$$\sum_{J\in S} \Phi_J(\mathbf{X}) = 1 \quad \sum_{J\in S} \nabla_0 \Phi_J(\mathbf{X}) = 0, \tag{22}$$

$$\sum_{J\in S} \Phi_J(\mathbf{X}) X_J = X \quad \sum_{J\in S} \Phi_J(\mathbf{X}) Y_J = Y \quad \sum_{J\in S} \Phi_J(\mathbf{X}) Z_J = Z. \tag{23}$$

Approximations that satisfy (22) have zeroth-order completeness. Since the approximation (21) does not fulfill zeroth-order completeness on the boundary even for a regular particle configuration, Monaghan [34] introduced a so called symmetrization. In this procedure he assumed that

$$\left(\sum_{J\in S} \nabla_0 W(\mathbf{X}_I - \mathbf{X}_J, h_0)V_J^0\right) u_I \equiv 0, \tag{24}$$

although this is only true for a uniform distribution of particles away from any boundary. Note that (24) is equivalent to assuming zeroth-order completeness (note the quantity inside the parenthesis in (24)). Adding Eq. (24) to Eq. (21) gives

$$\nabla u^h(\mathbf{X}_I) = -\sum_{J\in S} (u_J - u_I)\nabla_0 W(\mathbf{X}_I - \mathbf{X}_J, h_0)V_J^0. \tag{25}$$

A remarkable feature of the symmetrization procedure is that it yields zeroth-order completeness for the derivatives of a function for an irregular particle arrangement.

3.3. Krongauz–Belytschko correction

Johnson and Beissel [24] noted that errors in the extensional strains due to lack of linear completeness could be corrected by simple scaling, thus improving accuracy. A correction that enables the derivatives of

constant or linear fields to be reproduced exactly was developed by Randles and Libersky [41] and Krongauz and Belytschko [27]. We extend those ideas here to large deformations. The corrected derivatives are approximated by

$$\nabla_0 u^h(\mathbf{X},t) = \sum_{I\in S} \mathbf{G}_I(\mathbf{X}) u_I(t), \tag{26}$$

where $\mathbf{G}_I$ is a linear combination of the derivatives of the Shepard functions. $\mathbf{G}_I$ is obtained by a linear transformation

$$\mathbf{G}_I(\mathbf{X}) = \mathbf{a}(\mathbf{X}) \cdot \nabla_0 W_I^{\mathrm{S}}(\mathbf{X}), \tag{27}$$

where $\mathbf{a}(\mathbf{X})$ are arbitrary parameters and $W_I^{\mathrm{S}}(\mathbf{X})$ are the Shepard functions given by

$$W_I^{\mathrm{S}}(\mathbf{X}) = \frac{W_I(\mathbf{X})}{\sum_{I\in S} W_I(\mathbf{X})}. \tag{28}$$

Note that $\mathbf{a}(\mathbf{X})$ is invariant with respect to time for a Lagrangian kernel, so they need only be computed once and stored. The following reproducing condition for the derivative of a linear function must be fulfilled:

$$\sum_{I\in S} \mathbf{G}_I(\mathbf{X}) \otimes \mathbf{X}_I = \mathbf{I}, \tag{29}$$

where $\mathbf{I}$ is the identity matrix. Eq. (29) can be combined with (27) to yield

$$\sum_{I\in S} \mathbf{a}(\mathbf{X}) \cdot \nabla_0 W_I^{\mathrm{S}}(\mathbf{X}) \otimes \mathbf{X}_I = \mathbf{I}. \tag{30}$$

If we let $\mathbf{A}$ be the outer product of the derivatives of the Shepard function and $\mathbf{X}$

$$\mathbf{A} = \begin{bmatrix} W_{I,X}^{\mathrm{S}} X_I & W_{I,Y}^{\mathrm{S}} X_I & W_{I,Z}^{\mathrm{S}} X_I \\ W_{I,X}^{\mathrm{S}} Y_I & W_{I,Y}^{\mathrm{S}} Y_I & W_{I,Z}^{\mathrm{S}} Y_I \\ W_{I,X}^{\mathrm{S}} Z_I & W_{I,Y}^{\mathrm{S}} Z_I & W_{I,Z}^{\mathrm{S}} Z_I \end{bmatrix}$$

then (30) can be rewritten as

$$\mathbf{A}\mathbf{a}^{\mathrm{T}} = \mathbf{I}, \tag{31}$$

where

$$\mathbf{a} = \begin{bmatrix} a_{XX} & a_{XY} & a_{XZ} \\ a_{YX} & a_{YY} & a_{YZ} \\ a_{ZX} & a_{ZY} & a_{ZZ} \end{bmatrix}.$$

Thus, the parameters $\mathbf{a}$ can easily be determined from the set of three linear algebraic equation (31). Finally, we obtain the approximation for the derivatives of a function from (27) and (29) as

$$\nabla_0 u^h(\mathbf{X},t) = \sum_{I\in S} \mathbf{a}(\mathbf{X}) \cdot \nabla_0 W_I^{\mathrm{S}}(\mathbf{X}) u_I(t). \tag{32}$$

Since only the derivatives of the approximation are modified they are usually not integrable. Note that for Lagrangian kernels, the correction parameters $\mathbf{a}$ only need to be computed once.

Krongauz and Belytschko [27] showed that correction of the derivatives for both the test functions and the trial functions lead to a violation of the patch test. However, they showed that the patch test can be satisfied if Shepard functions are the test functions in a Petrov–Galerkin method. In this case, the test

functions do not meet linear completeness, so that global angular momentum is not conserved. However, in linear problems they observed excellent convergence. This procedure will herein be extended to large deformation problems.

3.4. Randles–Libersky correction

Randles et al. [41] developed a similar correction which they called normalization (NSPH). We develop it here for a Lagrangian kernel, which is a straightforward extension of their work. To fulfill the first-order completeness, they modified the SPH approximation for the gradient of the function u with a matrix $\mathbf{B}$:

$$\nabla u^h(\mathbf{X}_I,t)=\left(-\sum_{J\in S}(u_J(t)-u_I(t))\nabla_0 W(\mathbf{X}_I-\mathbf{X}_J,h_0)V_J^0\right)\cdot\mathbf{B}(\mathbf{X}_I) \tag{33}$$

with

$$\mathbf{B}(\mathbf{X})=\left(-\sum_{J\in S}(\mathbf{X}_J-\mathbf{X})\otimes\nabla_0 W(\mathbf{X}-\mathbf{X}_J,h_0)V_J^0\right)^{-1}. \tag{34}$$

A $\mathbf{B}$-matrix that correctly gives the derivatives of linear fields can also be considered using the Shepard function W^{S} instead of the symmetrization in (34). The expression for $\mathbf{B}$ becomes:

$$\mathbf{B}(\mathbf{X})=\left(-\sum_{J\in S}\mathbf{X}_J\otimes\nabla_0 W^{\mathrm{S}}(\mathbf{X}-\mathbf{X}_J,h_0)\right)^{-1}, \tag{35}$$

which is similar to the Krongauz–Belytschko correction [27]. There are subtle differences between (34) and (35). The approximation for the gradient of the function u can then be formulated in the unsymmetrized form because the Shepard functions are zeroth-order complete by construction:

$$\nabla u^h(\mathbf{X},t)=\left(-\sum_{J\in S}u_J(t)\nabla_0 W^{\mathrm{S}}(\mathbf{X}-\mathbf{X}_J,h_0)V_J^0\right)\cdot\mathbf{B}(\mathbf{X}). \tag{36}$$

3.5. The MLS-approximation

The MLS-approximation fulfills the reproducing conditions by construction, so no corrections are needed. The MLS approximation was introduced in the EFG-method by Nayroles et al. [36] and Belytschko et al. [5,31], and was first applied in a SPH setting by Dilts [16]. To satisfy the linear reproducing conditions linear base functions $\mathbf{p}$ are chosen to be

$$\mathbf{p}(\mathbf{X})=(1\ X\ Y\ Z)\quad\forall\mathbf{X}\in\Re^3. \tag{37}$$

The MLS approximation is

$$u^h(\mathbf{X},t)=\sum_{J\in S}\mathbf{p}_J(\mathbf{X})\mathbf{a}(\mathbf{X},t) \tag{38}$$

with $\mathbf{a}$ chosen to minimize

$$J=\sum_{J\in S}(\mathbf{p}_J(\mathbf{X})^{\mathrm{T}}\mathbf{a}(\mathbf{X},t)-u_J(t))^2 W(\mathbf{X}-\mathbf{X}_J,h). \tag{39}$$

Minimizing Eq. (39) with respect to **a** leads to the approximation

$$u^h(\mathbf{X},t) = \sum_{J\in S} u_J(t)\Phi_J(\mathbf{X}) \tag{40}$$

with

$$\Phi_J = \mathbf{p}(\mathbf{X})^{\mathrm{T}} \cdot \mathbf{A}(\mathbf{X})^{-1} \cdot \mathbf{p}_J(\mathbf{X}) W(\mathbf{X}-\mathbf{X}_J,h), \tag{41}$$

$$\mathbf{A}(\mathbf{X}) = \sum_{J\in S} \mathbf{p}_J(\mathbf{X})\mathbf{p}_J^{\mathrm{T}}(\mathbf{X}) W(\mathbf{X}-\mathbf{X}_J,h). \tag{42}$$

For zeroth-order completeness ($p(\mathbf{X}) = [1]$) the shape function Φ is

$$\Phi_J(\mathbf{X}) = \frac{W_{JI}}{\sum_{J\in S} W_{JI}}, \tag{43}$$

which is known as the Shepard function where $W_{JI} = W(\mathbf{X}_J - \mathbf{X}_I, h)$. A fast evaluation procedure for the gradient of the shape function Φ_J can be found in Belytschko et al. [3].

4. Discrete equations

4.1. Galerkin methods

4.1.1. The total Lagrangian formulation

In EFG, the discrete equations are obtained from a weak form of the momentum equation, which is given in the total Lagrangian description by

$$\int_{\Omega_0} \varrho_0 \delta\mathbf{u}\cdot\ddot{\mathbf{u}}\,\mathrm{d}\Omega_0 + \int_{\Omega_0} (\nabla_0\delta\mathbf{u})^{\mathrm{T}} : \mathbf{P}\,\mathrm{d}\Omega_0 - \int_{\Omega_0} \varrho_0\delta\mathbf{u}\cdot\mathbf{b}\,\mathrm{d}\Omega_0 - \int_{\Gamma_0^t} \delta\mathbf{u}\cdot\bar{\mathbf{t}}\,\mathrm{d}\Gamma = 0 \tag{44}$$

$\forall\delta\mathbf{u} \in V_0$ where V_0 is the space of test functions and $\mathbf{u} \in V$ where V is the space of trial functions. The spaces V_0 and V are as follows:

$$V = (\mathbf{u}(\mathbf{X},t) | \mathbf{u}(\mathbf{X},t) \in H^1(\Omega), \mathbf{u}(\mathbf{X},t) = \bar{\mathbf{u}} \quad \text{on } \Gamma_u), \tag{45}$$

$$V_0 = V \cap (\delta\mathbf{u}(\mathbf{X}) | \delta\mathbf{u}(\mathbf{X}) = 0 \quad \text{on } \Gamma_u). \tag{46}$$

The test and the trial functions are approximated by

$$\delta\mathbf{u}^h(\mathbf{X}) = \sum_{J\in S} \Phi_J(\mathbf{X})\delta\mathbf{u}_J, \tag{47}$$

$$\mathbf{u}^h(\mathbf{X},t) = \sum_{J\in S} \Psi_J(\mathbf{X})\mathbf{u}_J(t). \tag{48}$$

In a Petrov–Galerkin procedure, different approximating functions $\delta\mathbf{u}^h$ and $\mathbf{u}^h$ are chosen, so Φ_J differ from Ψ_J. We will use MLS shape functions (38) for the trial functions Ψ and Shepard functions for the test functions Φ. Furthermore, an assumed strain approach [44] is employed so that the gradient is approximated by (32). However, the formulation differs from [44] in that the gradient of the test function (not the assumed gradient) is used in computing the internal forces; Black and Belytschko [12] have given a convergence proof for this class of methods for the Laplace equation. Substituting (47) and (48) into (44) the discrete form of the momentum equation is obtained

$$\sum_J m_{IJ}\,\ddot{\mathbf{u}}_J = \mathbf{f}_I^{\mathrm{ext}} - \mathbf{f}_I^{\mathrm{int}}, \tag{49}$$

where $\mathbf{f}_I^{\text{ext}}$ and $\mathbf{f}_I^{\text{int}}$ are the external and the internal forces, given by

$$\mathbf{f}_I^{\text{ext}} = \int_{\Omega_0} \varrho_0 \Phi_I \mathbf{b}\, \mathrm{d}\Omega_0 + \int_{\Gamma_0^{\mathrm{t}}} \Phi_I \bar{\mathbf{t}}\, \mathrm{d}\Gamma_0, \tag{50}$$

$$\mathbf{f}_I^{\text{int}} = \int_{\Omega_0} \nabla_0 \Phi_I \cdot \mathbf{P}\, \mathrm{d}\Omega_0 \tag{51}$$

and

$$m_{IJ} = \sum_{I \in S} \int_{\Omega_0} \varrho_0 \Psi_I(\mathbf{X}) \Phi_J(\mathbf{X})\, \mathrm{d}\Omega_0. \tag{52}$$

The above mass matrix is the consistent mass matrix. It can be diagonalized by a row sum method (see e.g. [10]). However, in particle methods the diagonal mass is usually obtained by an ad hoc procedure. It is shown in Belytschko et al. [2] that if the test and the trial functions satisfy the linear reproducing conditions, then global linear and angular momentum are conserved. Bonet et al. [13] have also demonstrated this property.

As mentioned before, the standard derivation of SPH of the acceleration omits the time dependence of $\mathbf{x}_J(t)$ in (16). If we let

$$\mathbf{v}(\mathbf{x}, t) = \sum_{I \in S} W(\mathbf{x} - \mathbf{x}_I(t)) \mathbf{v}_I(t), \tag{53}$$

then the accelerations are

$$\mathbf{a} = \sum_{I \in S} W(\mathbf{x} - \mathbf{x}_I(t)) \dot{\mathbf{v}}_I + \nabla W(\mathbf{x} - \mathbf{x}_I(t)) \dot{\mathbf{x}}_I \cdot \mathbf{v}_I. \tag{54}$$

The second term is neglected in all versions of SPH that we know of, so it is also dropped in all calculations reported here.

4.1.2. The updated Lagrangian formulation

In the updated Lagrangian method, the weak form of the momentum equation is

$$-\int_{\Omega} (\nabla \delta \mathbf{v})^{\mathrm{T}} : \boldsymbol{\sigma}\, \mathrm{d}\Omega + \int_{\Omega} \delta \mathbf{v} \cdot (\varrho \mathbf{b} - \varrho \dot{\mathbf{v}})\, \mathrm{d}\Omega + \int_{\Gamma_t} \delta \mathbf{v} \cdot \bar{\boldsymbol{\tau}}\, \mathrm{d}\Gamma = 0. \tag{55}$$

Using the same procedure as for the total Lagrangian formulation, the discrete linear momentum equation for a Petrov–Galerkin method is

$$-\int_{\Omega} \nabla \Phi_J \cdot \boldsymbol{\sigma}\, \mathrm{d}\Omega + \int_{\Gamma_t} \Phi_J \bar{\boldsymbol{\tau}}\, \mathrm{d}\Gamma + \int_{\Omega} \varrho \Phi_J \mathbf{b}\, \mathrm{d}\Omega = \sum_I \int_{\Omega} \varrho \Phi_J(\mathbf{x}) \Psi_I(\mathbf{x})\, \mathrm{d}\Omega \frac{\mathrm{d}\mathbf{v}_I}{\mathrm{d}t}. \tag{56}$$

4.2. Collocation methods

In SPH, the discrete equations are obtained from the strong form by collocation, i.e. the governing equations are enforced at each particle. Neglecting body forces and boundary conditions, the momentum equation with the Lagrangian kernel is

$$m_I \ddot{\mathbf{u}} = V_I^0 \sum_{J \in S} V_J^0 \nabla_0 W_{IJ} \cdot \mathbf{P}_J. \tag{57}$$

In Eulerian coordinates the momentum equation is

$$m_I \dot{\mathbf{v}} = V_I \sum_{J \in S} V_J \nabla W_{IJ} \cdot \boldsymbol{\sigma}_J. \tag{58}$$

Usually the symmetrization given in Section 3.2 is applied to SPH methods. When the supports of all particles are of the same size, the above discrete SPH equations are equivalent to the discrete equations obtained from a nodal integration of the Galerkin form, except at the boundaries.

5. Integration schemes

5.1. Nodal integration

An efficient way to discretize the momentum equation in a Galerkin method is by nodal integration. In most computations of transient phenomena spatial integration by background cells is quite expensive. To obtain the discrete governing equations from the weak form, Beissel and Belytschko [1] proposed a nodal integration:

$$\int_{\Omega_0} f(\mathbf{X})\, \mathrm{d}\Omega_0 \approx \sum_{J \in S} f(\mathbf{X}_J) V_J^0, \tag{59}$$

where V_J^0 is the initial particle volume. Applying this technique to the computation of the internal forces (51) gives:

$$\mathbf{f}_I^{\mathrm{int}} = \sum_{J \in S} V_J^0 \nabla_0 \Phi_I(\mathbf{X}_J) \cdot \mathbf{P}_J. \tag{60}$$

The momentum equation is then

$$m_I \frac{\mathrm{d}\dot{\mathbf{u}}_I}{\mathrm{d}t} = \sum_{J \in S} (-\nabla_0 \Phi_I(\mathbf{X}_J) \cdot \mathbf{P}(\mathbf{X}_J) V_J^0 + \Phi_I(\mathbf{X}_J) \bar{\boldsymbol{\tau}}(\mathbf{X}_J) \Gamma_J^0 + \Phi_I(\mathbf{X}_J) \mathbf{b}(\mathbf{X}_J) \varrho(\mathbf{X}_J) V_J^0). \tag{61}$$

In Eulerian coordinates the momentum equation is

$$m_I \frac{\mathrm{d}\mathbf{v}_I}{\mathrm{d}t} = \sum_{J \in S} (-\nabla \Phi_I(\mathbf{x}_J) \cdot \boldsymbol{\sigma}(\mathbf{x}_J) V_J + \Phi_I(\mathbf{x}_J) \bar{\boldsymbol{\tau}}(\mathbf{x}_J) \Gamma_J + \Phi_I(\mathbf{x}_J) \mathbf{b}(\mathbf{x}_J) \varrho(\mathbf{x}_J) V_J). \tag{62}$$

5.2. Stress point integration

Stress point integration was proposed by Dyka et al. [18,19] to stabilize the SPH method. Randles et al. [42] extended stress point integration to higher dimensions to stabilize the normalized form of SPH. Stress point integration eliminates instabilities due to rank deficiency but not those due to the tensile instability, see Belytschko et al. [6].

In stress point integration methods, stress points are interspersed between the particles and the contributions of the stresses are added to the integration of (59) as described later. There are different methods for arranging the stress points between the original particles, see Belytschko et al. [6]. In the applications in this article, stress points are added as shown in Fig. 2. The additional stress points are only needed for the computation of the internal forces. All kinematic values at the stress points such as displacements and velocities are obtained from the original particles:

$$\mathbf{u}_I^{\mathrm{SP}} = \sum_{J \in S} \Phi_J(\mathbf{X}_I^{\mathrm{SP}}) \mathbf{u}_J^{\mathrm{P}}, \quad \mathbf{v}_I^{\mathrm{SP}} = \sum_{J \in S} \Phi_J(\mathbf{X}_I^{\mathrm{SP}}) \mathbf{v}_J^{\mathrm{P}}, \quad \nabla_0 \mathbf{v}_I^{\mathrm{SP}} = \sum_{J \in S} \mathbf{G}_J(\mathbf{X}_I^{\mathrm{SP}}) \mathbf{v}_J^{\mathrm{P}}, \tag{63}$$

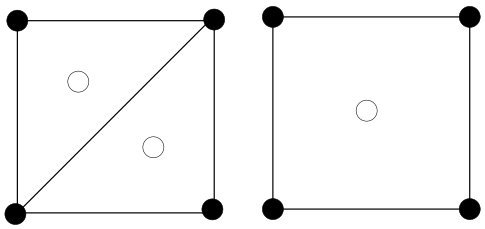

Fig. 2. Arrangement of the stress points.

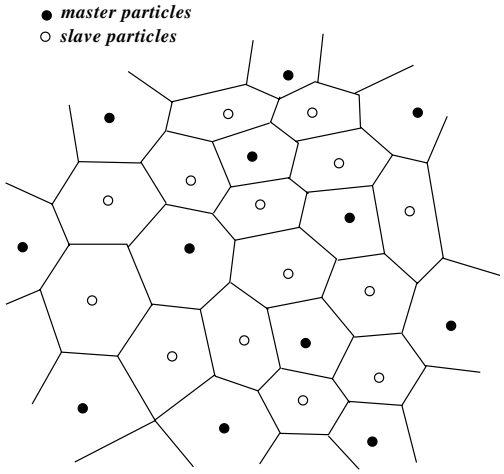

Fig. 3. Scheme of stress point integration.

where the superscript SP indicate stress points and the P the original particles. $\Phi_J(\mathbf{X}_I^{\mathrm{SP}})$ is the shape function value of the supporting master particle J at $\mathbf{X}_I^{\mathrm{SP}}$. Note that the displacements are approximated by the trial functions, whereas the gradient is obtained by the corrected derivatives.

The internal forces are calculated by

$$\mathbf{f}_I^{\mathrm{int}} = \sum_{J\in S} V_J^{0\mathrm{P}} \nabla_0 \Phi_I(\mathbf{X}_J^{\mathrm{P}}) \cdot \mathbf{P}(\mathbf{X}_J^{\mathrm{P}}) + \sum_{J\in S^{\mathrm{SP}}} V_J^{0\mathrm{SP}} \nabla_0 \Phi_I(\mathbf{X}_J^{\mathrm{SP}}) \cdot \mathbf{P}(\mathbf{X}_J^{\mathrm{SP}}), \tag{64}$$

where S^{SP} is the set of supporting stress points to the particle $\mathbf{X}_I^{\mathrm{P}}$. The volumes $V_J^{0\mathrm{P}}$ and $V_J^{0\mathrm{SP}}$ are computed from a Voronoi diagram (see Fig. 3) so that their sums give the total initial volume:

$$V^0 = \sum_J^{N_{\mathrm{P}}} V_J^{0\mathrm{P}} + \sum_J^{N_{\mathrm{S}}} V_J^{0\mathrm{SP}}, \tag{65}$$

where N_{P} is the number of particles and N_{S} is the number of stress points.

5.3. Cell integration

In EFG the integrals are usually evaluated over background cells based on an quadtree structure [5]. In each integration cell Gauss quadrature is performed. The number of Gauss points depends on the number of particles in a cell. Here, as in [5], at least $n_Q \times n_Q$ Gauss points are used with

$$n_Q = \sqrt{m} + 2, \tag{66}$$

where m denotes the number of particles in one cell.

In 2D the integral of a function is given by

$$\int_{\Omega_0} f(\mathbf{X})\,\mathrm{d}\Omega_0 = \int_{-1}^{+1}\int_{-1}^{+1} f(\xi,\eta)\det \mathbf{J}^{\xi}(\xi,\eta)\,\mathrm{d}\xi\,\mathrm{d}\eta = \sum_{J=1}^{m} w_J f(\boldsymbol{\xi}_J)\det \mathbf{J}^{\xi}(\boldsymbol{\xi}_J), \tag{67}$$

where $\boldsymbol{\xi} = (\xi,\eta)$ are scaled local coordinates, m is the total number of quadrature points, $w_J = w(\xi_J)w(\eta_J)$ are the quadrature weights which is the product of the weight at the corresponding Gauss point in ξ- and η-direction, and $\mathbf{J}^{\xi}$ is the Jacobian given by

$$\mathbf{J}^{\xi} = \frac{\partial \mathbf{X}}{\partial \boldsymbol{\xi}}. \tag{68}$$

The internal forces in 2D are then

$$\mathbf{f}^{\mathrm{int}} = \sum_{J=1}^{m} w_J \det \mathbf{J}^{\xi}(\boldsymbol{\xi}_J)\nabla_0 \Phi(\mathbf{X}(\boldsymbol{\xi}_J) - \mathbf{X}^{\mathrm{P}})\mathbf{P}(\boldsymbol{\xi}_J), \tag{69}$$

where the superscript P indicates the particle position.

6. Computation of the mass matrix

In dynamic problems with explicit time integration, a diagonal mass matrix is preferable for computational efficiency. A diagonal mass corresponds to assigning a mass to every particle. The masses are calculated in terms of nodal volumes obtained from a Voronoi diagram:

$$m_J = V_J^0 \varrho_J^0. \tag{70}$$

Crucial is how to consider and discretize the 'real' geometric volume of a body. It can be discretized with particles arranged as in Fig. 4(a) where the particles are inside the volume. No particles lie on the boundaries of the body. The body can also be discretized as illustrated in Fig. 4(b) where particles are placed exactly on the boundaries. For Fig. 4(a), all masses are equal; this leads to poor reflection conditions on boundaries. For the discretization in Fig. 4(b), the boundary particles have only half of the mass of the interior particles for a Voronoi method. The masses of the particles at the corners are only a quarter of the masses of the interior particles. We will show that this assignment of nodal masses leads to more accurate wave reflections.

The boundary integrals for natural boundary conditions (external forces) (50) also differ for the two models shown in Fig. 4. When the particles are located directly on the boundary, the value of the shape function differs from when the particles are at a certain distance from the boundaries (see Fig. 4).

7. Boundary conditions

In standard SPH, no conditions are imposed on stress free boundaries. This is sometimes considered justifiable because of compensating errors between the desired boundary conditions and errors in the boundary derivatives. It can also be justified by the integration by parts in the SPH derivation underlying (21) and the expression for the nodal forces, which is similar to the procedure in deriving a Galerkin weak form from the strong form. However, Randles and Libersky reported that SPH with corrected derivatives and no special treatment of boundary conditions led to errors. Traction boundary conditions in SPH are

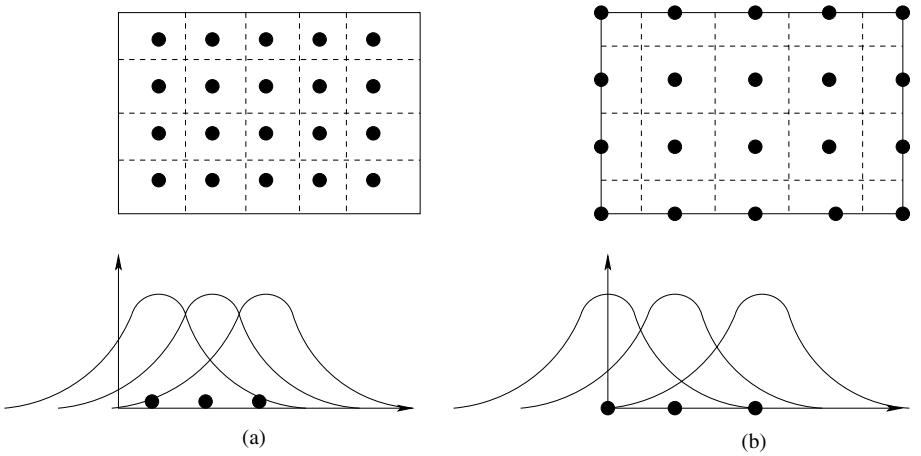

Fig. 4. Two arrangements of particles relative to a boundary and the corresponding shape functions.

investigated by Dilts [15,17] and Randles et al. [42]. We will show that the procedure developed here correctly treats traction-free boundaries.

8. A summary of particle methods

The standard SPH-procedure, a Randles–Libersky correction,a Krongauz–Belytschko correction and an MLS-approach have been reviewed. Many different discretizations can be constructed starting from these approximations by using a Petrov–Galerkin or Bubnov–Galerkin method or by point collocation (SPH). In the following we consider:

(1) The standard SPH-procedure with collocation (SPH).
(2) The Randles–Libersky correction with collocation (RLM ni).
(3) The Krongauz–Belytschko correction and Shepard functions in a Petrov–Galerkin method with nodal integration and stress points (KBM si).
(4) The EFG method with nodal integration (EFG ni).
(5) The EFG method with cell integration (EFG ci).

The equations for the internal forces and the deformation gradient are summarized in Table 1 for a Lagrangian kernel and in Table 2 for an Eulerian kernel. For the constitutive model in terms of the Eulerian kernel the velocity gradient $\mathbf{L}$ is given instead of the deformation gradient. As mentioned in Section 3.2, the equations can also be formulated in symmetrized versions. This is done for the SPH and the Randles–Libersky correction (RLM) shown in Tables 1 and 2, where $\mathbf{P}_I$ and $\boldsymbol{\sigma}_I$, respectively, are the stresses at the central particle.

9. Numerical results

9.1. Cantilever beam

In this section the cantilever beam illustrated in Fig. 5 is considered. Linear elastic material behavior is assumed. The beam is loaded with a parabolic traction at the end of the beam as shown in Fig. 5. The

Table 1
Discrete internal forces and deformation gradient for a Lagrangian kernel for various methods

	Internal forces	Deformation gradient
SPH	$\mathbf{f}_I^{\text{int}} = \sum_{J\in S}(\mathbf{P}_J + \mathbf{P}_I)\cdot\nabla_0 W_J V_J^0$	$\mathbf{F}_I = -\sum_{J\in S}(\mathbf{u}_J - \mathbf{u}_I)\otimes\nabla_0 W_J V_J^0$
	$f_{iI}^{\text{int}} = \sum_{J\in S}(P_{ij}(\mathbf{X}_J) + P_{ij}(\mathbf{X}_I))\dfrac{\partial W_J}{\partial X_j}V_J^0$	$F_{ijI} = -\sum_{J\in S}(u_{iJ} - u_{iI})\dfrac{\partial W_J}{\partial X_j}V_J^0$
RLM (ni)	$\mathbf{f}_I^{\text{int}} = \left(-\sum_{J\in S}(\mathbf{P}_J + \mathbf{P}_I)\otimes\nabla_0 W_J V_J^0\right):\mathbf{B}$	$\mathbf{F}_I = \left(-\sum_{J\in S}(\mathbf{u}_J - \mathbf{u}_I)\otimes\nabla_0 W_J V_J^0\right)\cdot\mathbf{B}$
	$f_{iI}^{\text{int}} = \left(-\sum_{J\in S}(P_{ij}(\mathbf{X}_J) + P_{ij}(\mathbf{X}_I))\dfrac{\partial W_J}{\partial X_k}V_J^0\right)B_{kj}$	$F_{ijI} = \left(-\sum_{J\in S}(u_{iJ} - u_{iI})\dfrac{\partial W_J}{\partial X_k}V_J^0\right)B_{kj}$
KBM (si)	$\mathbf{f}_I^{\text{int}} = \sum_{J\in S}\nabla_0 W_I^{\text{S}}(\mathbf{X}_J^{\text{P}})\cdot\mathbf{P}(\mathbf{X}_J^{\text{P}})V_J^{0\text{P}} + \sum_{J\in S^{\text{SP}}}\nabla_0 W_I^{\text{S}}(\mathbf{X}_J^{\text{SP}})\cdot\mathbf{P}(\mathbf{X}_J^{\text{SP}})V_J^{0\text{SP}}$	$\mathbf{F}^{\text{P}} = \sum_{J\in S}\mathbf{u}_J\otimes\mathbf{G}(\mathbf{X}_J^{\text{P}})$ $\mathbf{F}^{\text{SP}} = \sum_{J\in S^{\text{SP}}}\mathbf{u}_J\otimes\mathbf{G}(\mathbf{X}_J^{\text{SP}})$
	$f_{iI}^{\text{int}} = \sum_{J\in S}\dfrac{\partial W_I^{\text{S}}(\mathbf{X}_J^{\text{P}})}{\partial X_j}P_{ji}(\mathbf{X}_J^{\text{P}})V_J^{0\text{P}} + \sum_{J\in S^{\text{SP}}}\dfrac{\partial W_I^{\text{S}}(\mathbf{X}_J^{\text{SP}})}{\partial X_j}P_{ji}(\mathbf{X}_J^{\text{SP}})V_J^{0\text{SP}}$	$F_{ij}^{\text{P}} = \sum_{J\in S}u_{iJ}G_j(\mathbf{X}_J^{\text{P}})$ $F_{ij}^{\text{SP}} = \sum_{J\in S^{\text{SP}}}u_{iJ}G_j(\mathbf{X}_J^{\text{SP}})$
EFG (ni)	$\mathbf{f}_I^{\text{int}} = \sum_{J\in S}\mathbf{P}_J\cdot\nabla_0\Phi_I(\mathbf{X}_J)V_J^0$	$\mathbf{F}_I = -\sum_{J\in S}(\mathbf{u}_J - \mathbf{u}_I)\otimes\nabla_0\Phi_I(\mathbf{X}_J)$
	$f_{iI}^{\text{int}} = \sum_{J\in S}P_{ij}(\mathbf{X}_J)\dfrac{\partial\Phi_I(\mathbf{X}_J)}{\partial X_j}V_J^0$	$F_{ijI} = -\sum_{J\in S}(u_{iJ} - u_{iI})\dfrac{\partial\Phi_I(\mathbf{X}_J)}{\partial X_j}$
EFG (ci)	$\mathbf{f}_I^{\text{int}} = \sum_{J=1}^{m} w_J\det\mathbf{J}_J^{\xi}\mathbf{P}_J\cdot\nabla_0\Phi(\mathbf{X}_J - \mathbf{X}_I^{\text{P}})$	$\mathbf{F}_I = \sum_{J=1}^{N_{\text{P}}}\mathbf{u}_J\otimes\nabla_0\Phi(\mathbf{X}_I^{GP} - \mathbf{X}_J)$
	$f_{iI}^{\text{int}} = \sum_{J=1}^{m} w_J\det\mathbf{J}_J^{\xi}P_{ij}(\mathbf{X}_J)\dfrac{\partial\Phi(\mathbf{X}_J - \mathbf{X}_I^{\text{P}})}{\partial X_j}$	$F_{ijI} = \sum_{J=1}^{N_{\text{P}}}u_{iJ}\dfrac{\partial\Phi(\mathbf{X}_I^{GP} - \mathbf{X}_J)}{\partial X_j}$

$W_J = W(\mathbf{X}_I - \mathbf{X}_J)$, $\Phi_I(\mathbf{X}_J) = \Phi(\mathbf{X}_I - \mathbf{X}_J)$, $\mathbf{P}_J = \mathbf{P}(\mathbf{X}_J)$, etc.
SPH—symmetrized SPH with collocation
RLM (ni)—Randles–Libersky correction with nodal integration
KBM (si)—Krongauz–Belytschko correction with stress point integration
EFG (ni)—EFG with nodal integration, EFG (ci)—EFG with cell integration

analytic solution for this problem can be found in [21]. The five methods summarized in Section 8 are considered. The normalized L_2 error in the displacement as well as the error in the energy is checked. The normalized L_2 error in the displacement is computed by

$$\|\text{err}\|_{L_2} = \frac{\|\mathbf{u}^h - \mathbf{u}_{\text{analytic}}\|_{L_2}}{\|\mathbf{u}_{\text{analytic}}\|_{L_2}} \tag{71}$$

with

$$\|\mathbf{u}\|_{L_2} = \sqrt{\int_{\Omega_0}\mathbf{u}\cdot\mathbf{u}\,\mathrm{d}\Omega_0}. \tag{72}$$

The error in the energy is obtained by

$$\|\text{err}\|_{\text{energy}} = \frac{\|\mathbf{u}^h - \mathbf{u}_{\text{analytic}}\|_{\text{energy}}}{\|\mathbf{u}_{\text{analytic}}\|_{\text{energy}}} \tag{73}$$

with

$$\|\mathbf{u}\|_{\text{energy}} = \int_{\Omega_0}\mathbf{P}:\mathbf{F}^{\text{T}}\,\mathrm{d}\Omega_0. \tag{74}$$

The integrals are evaluated numerically by the procedure that is used to evaluate the nodal forces, i.e. by Gauss quadrature in EFG. The results are presented in Fig. 6. The best results are obtained with EFG with

Table 2
Discrete internal forces and deformation gradient for an Eulerian kernel for various methods

	Internal forces	Velocity gradient
SPH	$\mathbf{f}_I^{\text{int}} = \sum_{J\in S}(\boldsymbol{\sigma}_J + \boldsymbol{\sigma}_I)\cdot\nabla W_J V_J$	$\mathbf{L}_I = -\sum_{J\in S}(\mathbf{v}_J - \mathbf{v}_I)\otimes\nabla W_J V_J$
	$f_{iI}^{\text{int}} = \sum_{J\in S}(\sigma_{ij}(\mathbf{x}_J) + \sigma_{ij}(\mathbf{x}_I))\dfrac{\partial W_J}{\partial x_j}V_J$	$L_{ijI} = -\sum_{J\in S}(v_{iJ} - v_{iI})\dfrac{\partial W_J}{\partial x_j}V_J$
RLM (ni)	$\mathbf{f}_I^{\text{int}} = \left(-\sum_{J\in S}(\boldsymbol{\sigma}_J + \boldsymbol{\sigma}_I)\otimes\nabla W_J V_J\right):\mathbf{B}$	$\mathbf{L}_I = \left(-\sum_{J\in S}(\mathbf{v}_J - \mathbf{v}_I)\otimes\nabla W_J V_J\right)\cdot\mathbf{B}$
	$f_{iI}^{\text{int}} = \left(-\sum_{J\in S}(\sigma_{ij}(\mathbf{x}_J) + \sigma_{ij}(\mathbf{x}_I))\dfrac{\partial W_J}{\partial x_k}V_J\right)B_{kj}$	$L_{ijI} = \left(-\sum_{J\in S}(v_{iJ} - v_{iI})\dfrac{\partial W_J}{\partial x_k}V_J\right)B_{kj}$
KBM (si)	$\mathbf{f}_I^{\text{int}} = \sum_{J\in S}\nabla W_I^{\text{S}}(\mathbf{x}_J^{\text{P}})\cdot\boldsymbol{\sigma}(\mathbf{x}_J^{\text{P}})V_J^{\text{P}} + \sum_{J\in S^{\text{SP}}}\nabla W_I^{\text{S}}(\mathbf{x}_J^{\text{SP}})\cdot\boldsymbol{\sigma}(\mathbf{x}_J^{\text{SP}})V_J^{\text{SP}}$	$\mathbf{L}^{\text{P}} = \nabla\otimes\mathbf{v}^{\text{P}} = \sum_{J\in S}\mathbf{v}_J\otimes\mathbf{G}(\mathbf{x}_J^{\text{P}})$
		$\mathbf{L}^{\text{SP}} = \nabla\otimes\mathbf{v}^{\text{SP}} = \sum_{J\in S^{\text{SP}}}\mathbf{v}_J\otimes\mathbf{G}(\mathbf{x}_J^{\text{SP}})$
	$f_{iI}^{\text{int}} = \sum_{J\in S}\dfrac{\partial W_I^{\text{S}}(\mathbf{x}_J^{\text{P}})}{\partial x_j}\sigma_{ji}(\mathbf{x}_J^{\text{P}})V_J^{\text{P}} + \sum_{J\in S^{\text{SP}}}\dfrac{\partial W_I^{\text{S}}(\mathbf{x}_J^{\text{SP}})}{\partial x_j}\sigma_{ji}(\mathbf{x}_J^{\text{SP}})V_J^{\text{SP}}$	$L_{ij}^{\text{P}} = \sum_{J\in S}v_{iJ}G_j(\mathbf{x}_J^{\text{P}})$
		$L_{ij}^{\text{SP}} = \sum_{J\in S^{\text{SP}}}v_{iJ}G_j(\mathbf{x}_J^{\text{SP}})$
EFG (ni)	$\mathbf{f}_I^{\text{int}} = \sum_{J\in S}\boldsymbol{\sigma}_J\cdot\nabla\Phi_I(\mathbf{x}_J)V_J$	$\mathbf{L}_I = -\sum_{J\in S}(\mathbf{v}_J - \mathbf{v}_I)\otimes\nabla\Phi_I(\mathbf{x}_J)$
	$f_{iI}^{\text{int}} = \sum_{J\in S}\sigma_{ij}(\mathbf{x}_J)\dfrac{\partial\Phi_I(\mathbf{x}_J)}{\partial x_j}V_J$	$L_{ijI} = -\sum_{J\in S}(v_{iJ} - v_{iI})\dfrac{\partial\Phi_I(\mathbf{x}_J)}{\partial x_j}$
EFG (ci)	$\mathbf{f}_I^{\text{int}} = \sum_{J=1}^{m}w_J\det\mathbf{J}_J^{\xi}\boldsymbol{\sigma}_J\cdot\nabla\Phi(\mathbf{x}_J - \mathbf{x}_I^{\text{P}})$	$\mathbf{L}_I = \sum_{J=1}^{N_{\text{P}}}\mathbf{v}_J\otimes\nabla\Phi(\mathbf{x}_I^{GP} - \mathbf{x}_J)$
	$f_{iI}^{\text{int}} = \sum_{J=1}^{m}w_J\det\mathbf{J}_J^{\xi}\sigma_{ij}(\mathbf{x}_J)\dfrac{\partial\Phi_I(\mathbf{x}_J - \mathbf{x}_I^{\text{P}})}{\partial x_j}$	$L_{ijI} = \sum_{J=1}^{N_{\text{P}}}v_{iJ}\dfrac{\partial\Phi_I(\mathbf{x}_I^{GP} - \mathbf{x}_J)}{\partial x_j}$

$W_J = W(\mathbf{x}_I - \mathbf{x}_J)$, $\Phi_I(\mathbf{x}_J) = \Phi(\mathbf{x}_I - \mathbf{x}_J)$, $\boldsymbol{\sigma}_J = \boldsymbol{\sigma}(\mathbf{x}_J)$, etc.
SPH—symmetrized SPH with collocation
RLM (ni)—Randles–Libersky correction with nodal integration
KBM (si)—Krongauz–Belytschko correction with stress point integration
EFG (ni)—EFG with nodal integration, EFG (ci)—EFG with cell integration

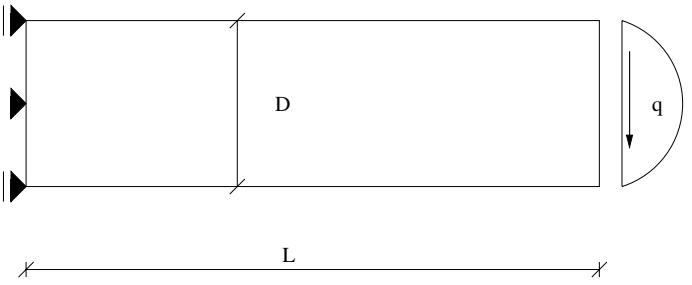

Fig. 5. Model for the cantilever beam.

cell integration. The Randles–Libersky and Krongauz–Belytschko corrections combined with a nodal integration yield poor results. We have not considered the Randles–Libersky method with stress points which would probably perform like the Krongauz–Belytschko correction with stress points.

SPH does not converge at all; this is a striking result that was also observed in Belytschko et al. [2]. Convergence for SPH can be achieved if the domain of influence is kept constant during refinement. Fig. 7(a) shows the error in the displacement norm, Fig. 7(b) shows the error in the energy norm for SPH and EFG with cell integration if the domain of influence is kept constant when refining the discretization. Note

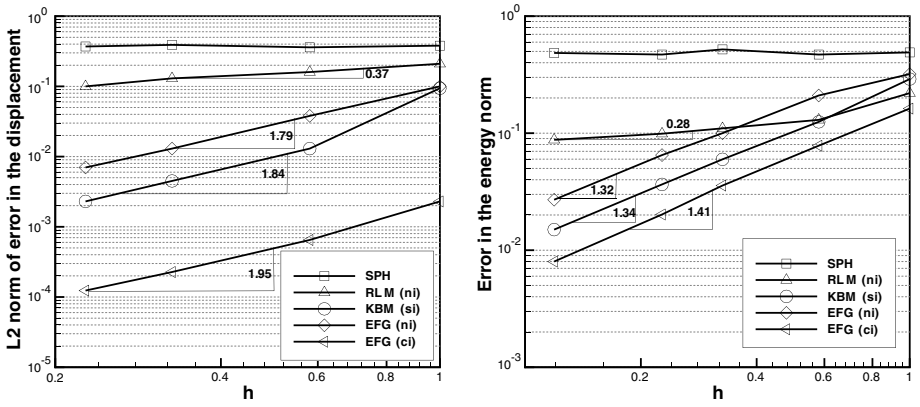

Fig. 6. L_2 norm of error in displacement and error in energy for different particle methods, see Section 8 for nomenclature.

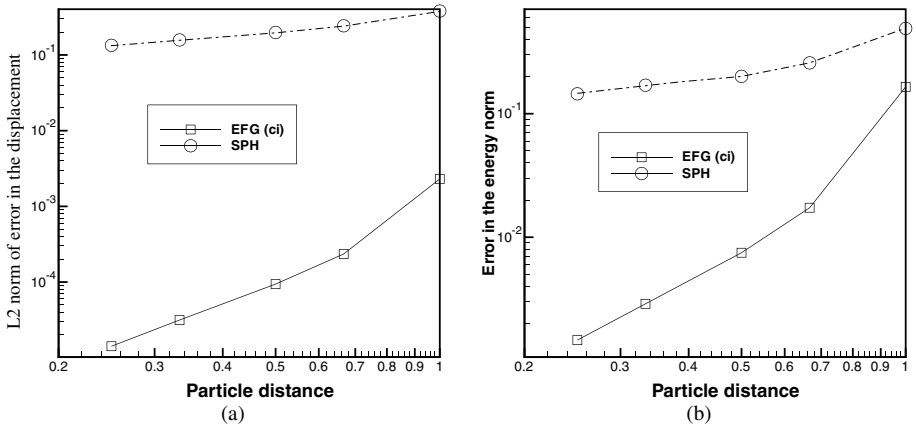

Fig. 7. (a) L_2 norm of error in displacement and (b) error in energy for EFG with cell integration and SPH and a constant domain of influence.

that the EFG results are also more accurate for large R (R is the distance of the particles); compare Figs. 6 and 7. It should be mentioned that for practical reasons the domain of influence cannot be kept constant during refinement since too many particles will contribute to the sum which increases the computational cost enormously.

EFG with nodal integration and the Krongauz–Belytschko method with stress point integration provide pretty good results. The rate of convergence is only a little bit less than for EFG with a cell integration, but the relative error is larger.

9.2. Linear elastic rod with initial displacement

To investigate these methods for wave propagation and reflection, another simple example is studied: a linear elastic rod. The major aim here is to examine the effect of the mass lumping described in Section 6. The rod is discretized in 2D (plane strain). It is 60 mm long and its height is 5 mm. Again, the five methods summarized in Section 8 are investigated. A rectangular impulse with a velocity of 50 m/s is applied to the left hand end for 5.8 ms. The same number of particles (number of particles = 19,721) is used in the

numerical simulation. This correspond to 481 particles in x-direction. The particle separation is 0.125 mm; Young's modulus $E = 210,000$ and Poisson's ratio $v = 0.0$. The L_2 error in the velocities is given before and after the wave reflection:

$$\|\mathrm{err}\|_{L_2} = \frac{\|\mathbf{v}^h - \mathbf{v}_{\mathrm{analytic}}\|}{\|\mathbf{v}_{\mathrm{analytic}}\|}. \tag{75}$$

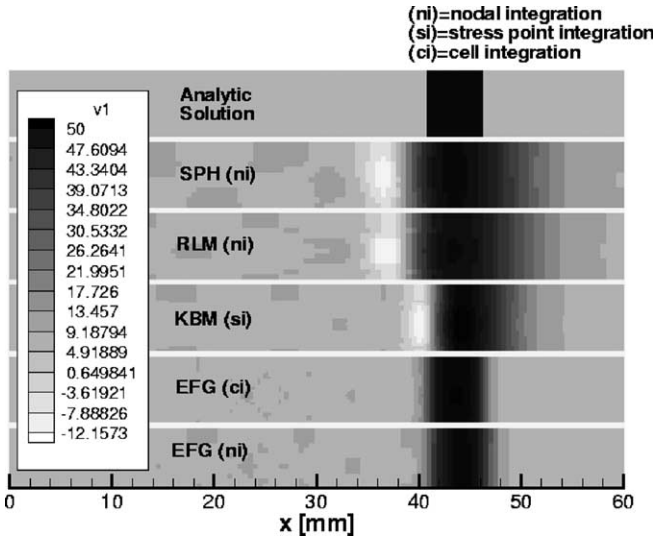

Fig. 8. Velocity field in the rod for a rectangular impulse for different particle methods and integration schemes before the wave reflection.

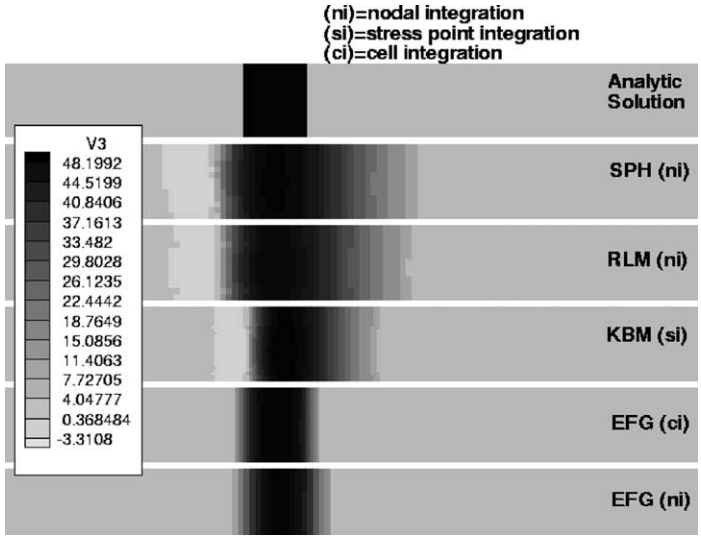

Fig. 9. Velocity field in the rod for a rectangular impulse for different particle methods and integration schemes after the second wave reflection.

In Fig. 8 the velocity is shown for the rectangular impulse before the wave reflection. Fig. 9 shows the velocity after the wave reflects from the left-hand side. The best resolution is obtained by EFG with full quadrature, but EFG with nodal quadrature is also able to reproduce the analytic velocity field quite well. For SPH and the Randles–Libersky correction (we did not include the explicit enforcement of traction boundary conditions that Randles and Libersky advocate), some oscillations before the maximum pressure peak can be observed, which results in a significantly higher error. It should be mentioned that different artificial viscosities with different damping factors were tried to keep the wave dispersion as small as possible.

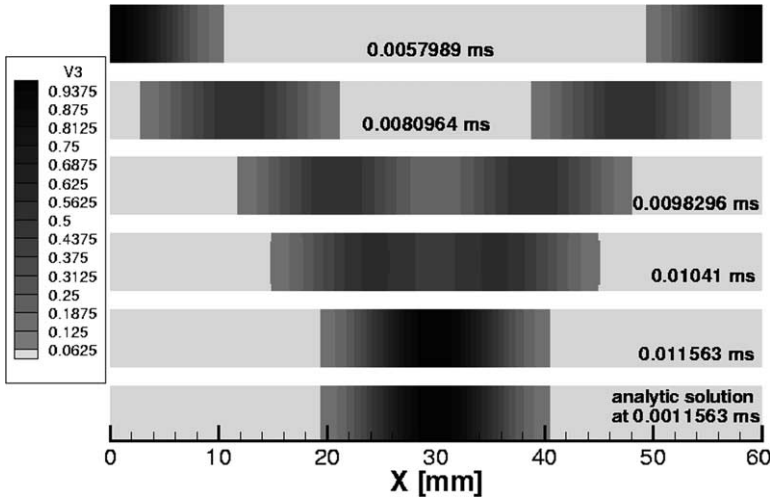

Fig. 10. Velocity profiles in the rod for an initial velocity condition (Gauss distribution of the velocities) for EFG with cell integration at different times.

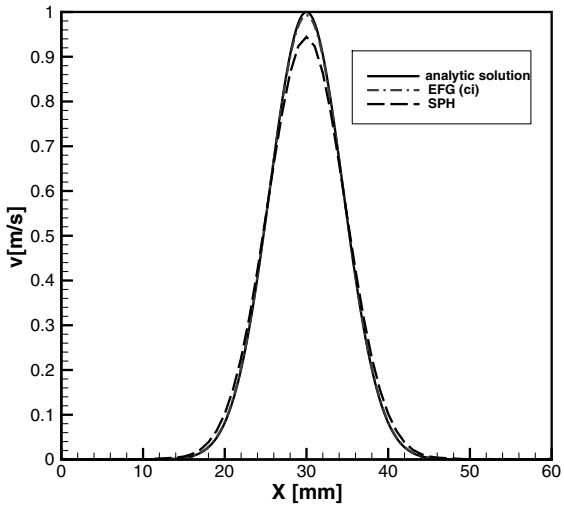

Fig. 11. Velocity profile in the middle of the rod for SPH and EFG with cell integration compared to the analytical solution at $t = 0.011563$ ms.

Next, an initial velocity of $v = e^{(-\alpha(x-30)^2)}$, $\alpha = 0.025$ was prescribed. The sound speed is $c = \sqrt{E/\varrho}$ with $E = 210,000$ MPa and $\varrho = 0.0078$ g/mm^3, so the wave returns to its original position at $t = 0.011563$ ms. Fig. 10 shows the velocity field at different times for EFG with cell integration. It can be seen how the wave propagates to the left and right hand ends, is reflected and after 0.011563 ms reaches its original position again. Fig. 11 illustrates the velocity field at $t = 0.011563$ ms for a section in the middle of the rod for SPH and EFG with cell integration compared to the analytical solution. As can be seen, the EFG simulation and the analytic solution match almost exactly. The wave dispersion is greater for SPH. Also, the maximum velocity is not reached for the SPH computation. In Table 3, the error in the velocity is given for the different methods at two times. At $t = 0.011563$ ms, the wave first reaches its original position, at $t = 0.023126$ ms it reaches its original position for the second time. As expected, the best results are obtained with EFG and cell integration; for SPH the error is approximately 5% (see Table 3).

Table 3 gives also the computation times for the different particle methods. Approximately 2500 time steps were needed for the computation. The computations were performed on an IBM RS6000SP-SMP with 192 Gflop/s performance. The longest computation is the EFG with cell integration.

9.3. Notched concrete beam in bending

This example is an unreinforced notched concrete beam under a static load as shown in Fig. 12, see Peterson [38]. The beam is 2 m long and has a rectangular cross section 20 and 10 cm in height and depth, respectively. In the middle, the beam has a 4 cm wide notch over half the height of the cross section. The initial elastic modulus is 30,000 MPa and the concrete tensile strength is 3.3 MPa. The constitutive model for concrete is a combined damage plasticity model as proposed in Rabczuk and Eibl [40]. It was originally developed by Schmidt–Hurtienne [43] and modified in some points. The material parameters are listed in Table 4. A Lagrangian kernel was used. The beam was discretized with 396,000 particles. The load was

Table 3
L_2 error in the velocities for an initial condition (Gauss distribution of the velocities) for different particle methods before and after the wave reflection

	Error at 0.0116 ms	Error at 0.0231 ms	Number of particles	Number of str. points	Number of cells	CPU time (min)
SPH (ni)	0.05026	0.04999	20,000	–	–	6.2
RLM (ni)	0.01301	0.01297	20,000	–	–	7.8
KBM (si)	0.00813	0.00842	10,500	10,200	–	8.4
EFG (ni)	0.008322	0.008232	20,000	–	–	7.6
EFG (ci)	0.006817	0.006834	4100	–	15,700	20.1

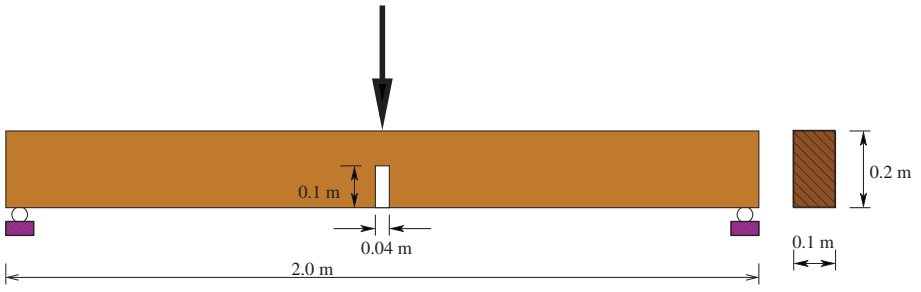

Fig. 12. Notched unreinforced concrete beam of Peterson [38] under static concentrated loading.

Table 4
Material parameters of the constitutive model for concrete

$E_0 = 30,000$ MPa	$e_0 = 2.5 \times 10^{-5}$	$e_{p2} = 0,4$
$v = 0.22$	$e_d = 2.2 \times 10^{-4}$	$\varrho = 2.4 \times 10^{-3}$
$c_1 = 0.0123424$	$g_d = 1.5$	$n_{\text{dam}} = 70$
$c_2 = 0.025166$	$r_t = 1.2$	$a_v = 0.7$
$c_3 = 0.782058$	$r_c = 100$	$b_v = 3.5$
$c_4 = 0.346384$	$c_p = 0.9$	$e_v = 0.02$
$c_c = 0.08$	$e_{p1} = 1.1 \times 10^{-3}$	$e_{v,th} = 0.008$

applied as a linear function in time in the middle of the beam, so that the strain rate does not exceed 1×10^{-6}/s.

Fig. 13 compares the experimental load–midpoint displacement curves to the simulations with different numbers of particles. In addition, the influence of the different methods is shown for the fine mesh. It can be seen that the EFG method provides the best results, but the Krongauz–Belytschko method also reproduces the experimental data quite well. The SPH results, for a reason we cannot explain, decay much faster than the experimental results. Nevertheless, the influence of the numerics does not seem to be very high. Overall, it can be said that the experimental results can be reproduced reasonably well, without spurious discretization dependence. The results for an Eulerian and Lagrangian kernel gave almost identical results. We did not observe any tensile instabilities in SPH which is expected because of the low tensile strength of concrete.

For this example we will discuss the computational efficiency of the particle methods. We used 20 processors and a parallelization technique described in [39]. Approximately 12,000 time steps were needed for the computation. Except for the full Gauss quadrature, the computation time for the different particle methods do not differ too much when a Lagrangian kernel is used (see Table 5). Since for a Lagrangian kernel the shape functions are computed only once and a neighbor search is performed only at the beginning of the computation, the Lagrangian kernels perform better than the Eulerian kernel. For an Eulerian kernel the neighbor search is performed every thirtieth time step. The most important factor is the

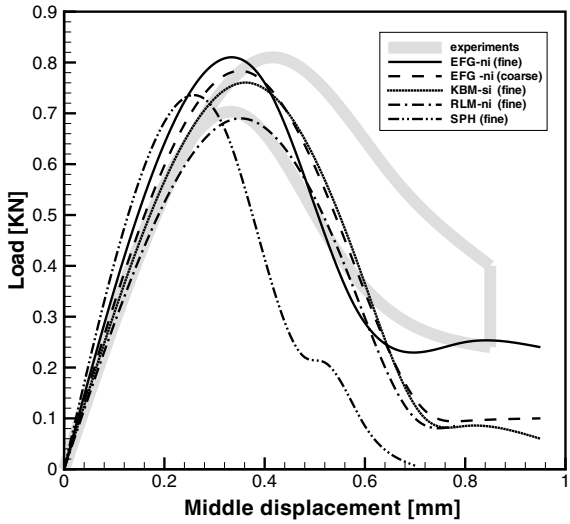

Fig. 13. Load–middle displacement curves of the experiment (the two curves give the range of results) of Peterson [38] compared with the numerical results.

Table 5
Computation times for a Lagrangian kernel for 12,000 time steps

Method	Number of particles	Number of stress points	Number of Gauss points	Total CPU time (CPU h)
SPH (ni)	396,000	–	–	34.8
RLM (ni)	396,000	–	–	39.5
KBM (si)	175,000	173,000	–	39.3
EFG (ni)	396,000	–	–	38.2
EFG (ci)	43,000	–	340,000	68.7

Table 6
Computation times for an Eulerian kernel for 12,000 time steps

Method	Number of particles	Number of stress points	Number of Gauss points	Total CPU time (CPU h)
SPH (ni)	396,000	–	–	36.8
RLM (ni)	396,000	–	–	45.0
KBM (si)	175,000	173,000	–	48.3
EFG (ni)	396,000	–	–	84.0

number of computation of the shape functions, as can be seen from Tables 5 and 6. The CPU time for EFG with nodal integration is twice that for SPH. Also the CPU-time for the Randles–Libersky and Krongauz–Belytschko method is somewhat greater but not as severely.

9.4. Shear band propagation in metals

We next consider the simulation of shear band development in metals. The KBM with stress point integration was used with Eulerian and Lagrangian kernel. Shear band formation is related to material instabilities, so this is an area where Lagrangian kernels are expected to perform better. A square plate under compressive load is considered. A viscoplastic constitutive model as described by Needleman [37] was used. The model description and parameters can be found in Belytschko et al. [11] and in Fig. 14. The plate is discretized with 250,000 particles. Fig. 16 shows the effective plastic strain (in [%]) in the specimen at

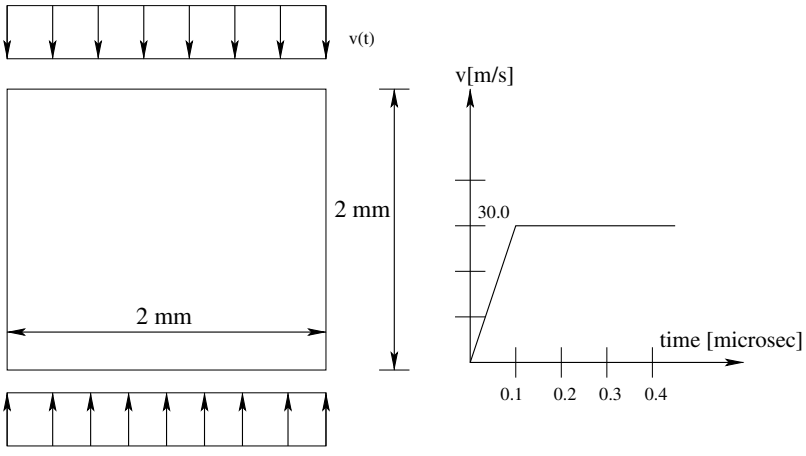

Fig. 14. Model description for the quadratic plate under compression.

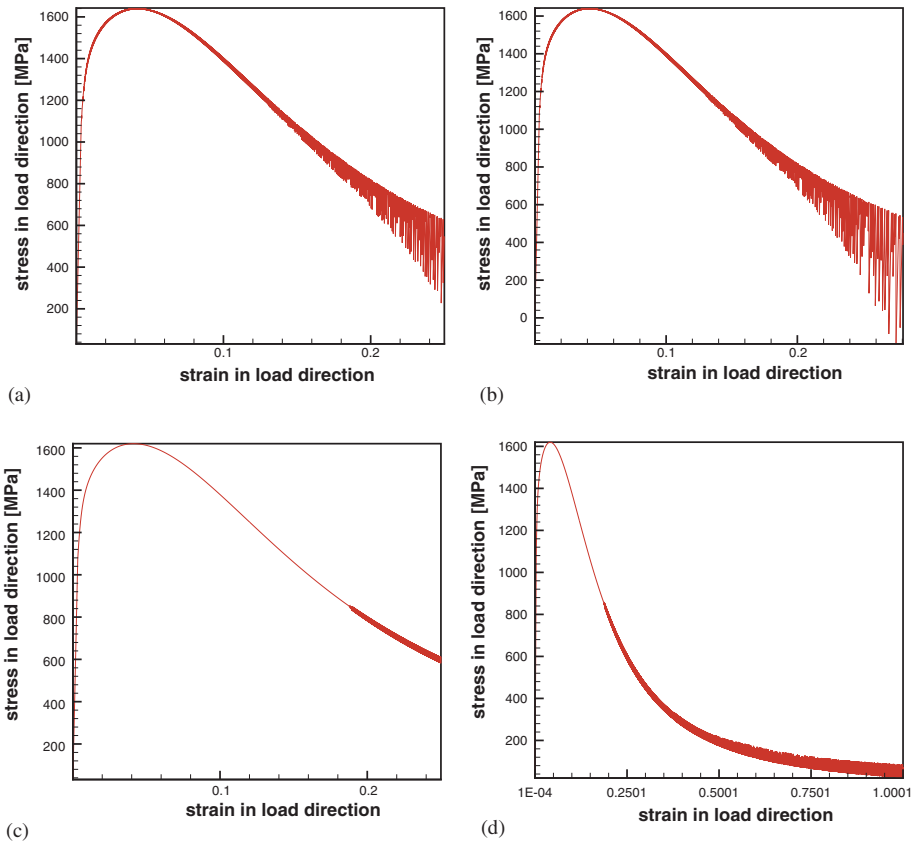

Fig. 15. Stress–strain curve of the viscoplastic model with (a) and (b) for an Eulerian and (c) and (d) for a Lagrangian kernel.

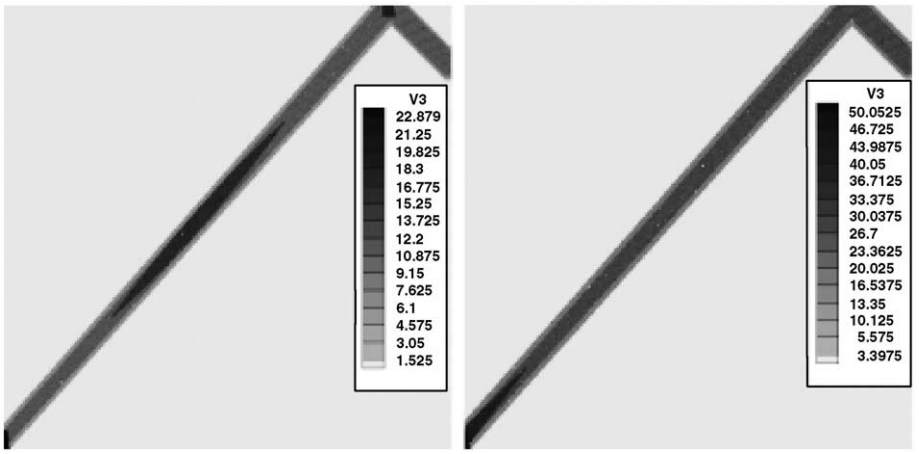

Fig. 16. Effective plastic strain of the plate under compressive loading to different time steps.

different time steps. They are in good agreement with the results obtained by Needleman [37] and Belytschko et al. [11]. Fig. 15 illustrates the stress strain behavior for a particle in the middle of the shear band. With an Eulerian kernel, the calculations evidences an instability in the softening domain; continuing the calculations leads to further growth of the oscillations. This instability wasn't observed for a Lagrangian kernel with stress points, see Fig. 15(c) and (d), although some slightly increasing oscillations are apparent.

9.5. Shear bands in rings

Here we will examine the performance of Lagrangian and Eulerian kernels for a problem exhibiting several shear bands. The Krongauz–Belytschko method with stress point integration is used. A J_2 flow constitutive model is applied and the stress rate relation is

$$\boldsymbol{\tau}^{\nabla J} = C_{\mathrm{el}}^{\tau J} : \mathbf{D}^e = C_{\mathrm{el}}^{\tau J} : (\mathbf{D} - \mathbf{D}^p), \tag{76}$$

where $\boldsymbol{\tau}$ is the Kirchhoff stress computed by $\boldsymbol{\tau} = \mathbf{F} \cdot \mathbf{P}$. The yield condition is

$$f(\boldsymbol{\tau}, \mathbf{q}) = \bar{\sigma} - \sigma_{\mathrm{Y}}(\bar{\epsilon}) = 0,$$

$$\frac{\partial f}{\partial \boldsymbol{\tau}} = \frac{3}{2\bar{\sigma}} \boldsymbol{\tau}^{\mathrm{dev}} \quad \frac{\partial f}{\partial \bar{\epsilon}} = -\frac{\mathrm{d}}{\mathrm{d}\bar{\epsilon}} \sigma_{\mathrm{Y}}(\bar{\epsilon}) = -H(\bar{\epsilon}),$$

where $\sigma_{\mathrm{Y}}(\bar{\epsilon})$ is the yield stress in uniaxial tension, $\bar{\epsilon}$ is the effective plastic strain, $\bar{\sigma}$ is the von Mises effective stress $[\frac{3}{2}\boldsymbol{\tau}^{\mathrm{dev}} : \boldsymbol{\tau}^{\mathrm{dev}}]^{1/2}$, $\boldsymbol{\tau}^{\mathrm{dev}}$ is the deviatoric stress and $H(\bar{\epsilon})$ is the plastic modulus. For strain softening, H is negative.

The steel ring is loaded along the inner ring. A pressure of 1.0e10 N/m^2 is first applied and is then decreased exponentially in time. The material constants are $\rho = 7800$ kg/m^3, $E = 2.0\mathrm{e}11$ N/m^2, $H = -E/10$, $\sigma_{\mathrm{Y}}(0) = 1.0\mathrm{e}10$ N/m^2. One thousand and fifty particles and 900 stress points are used.

Fig. 17 shows the distribution of the effective strain in the deformed steel ring. The shear bands occur because of the unstable material behavior. According to [26], the field of shear bands around a circular hole loaded by a uniform pressure is known since at every point of the field the principal stress coincides with the radial and peripheral directions. The shear bands will be logarithmic spirals emerging from the inner surface at an angle $\pm\frac{\pi}{4}$.

Regardless of whether we use a Lagrangian or an Eulerian kernel, the shear bands have the above mentioned morphology. When a shear band has grown through the ring, the ring breaks into fragments [22,23,35].

The shear bands usually are initiated where stress or strain concentrations occur due to geometric or material inhomogeneities. In a numerical simulation with uniformly distributed stresses, a slight imperfection

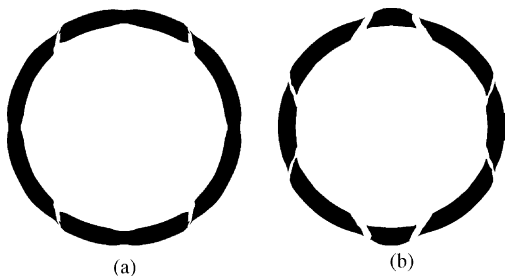

Fig. 17. Deformed steel ring by stress points ($t = 0.5$ ms): (a) Lagrangian kernal and (b) Eulerian kernal.

from either the material or the numerics may trigger the localization. So shear bands will occur at different positions in different patterns for different models. With an Eulerian kernel, the positions of the shear bands differ from those in Lagrangian kernel simulation but it may simply be a reflection of these effects. The response observed for the Eulerian kernel is quite acceptable. This is not always the case, as shown in the next example.

9.6. Spurious material instability

This example shows the onset of a spurious instability for an Eulerian kernel in a 2D problem. Again, the KBM with stress point integration is applied with Eulerian and Lagrangian kernels. The material model is given in Eq. (18) and the related text. This material was studied in Xiao et al. [47] where it was shown analytically that stress point integration with Lagrangian kernels can reproduce the material instability but Eulerian kernels distort it severely.

A pressure of 6.2e7 N/m^2 is applied for 0.1 ms on the inner surface of the rubber ring. The discrete model with stress points consists of 540 particles and 480 stress points. Fig. 18 shows the deformed rubber ring at the same time for the Lagrangian kernel and an Eulerian kernel computations. Fig. 18(b) exhibits a clustering of particles in the Eulerian kernel which is typical of the tensile instability. Fig. 19 shows the distribution of $\sigma_{\theta\theta}$ in the deformed configuration. As can be seen, the stress is concentrated at discrete locations around the circumference of the ring for the Eulerian kernel but it is still rotationally symmetric for the Lagrangian kernel.

9.7. Fluid flow in a funnel

To illustrate a problem where the Eulerian kernel is more suitable than the Lagrangian kernel consider a fluid flow in a funnel. The KBM with stress point integration is used. The material behavior of the fluid is described via an equation of state:

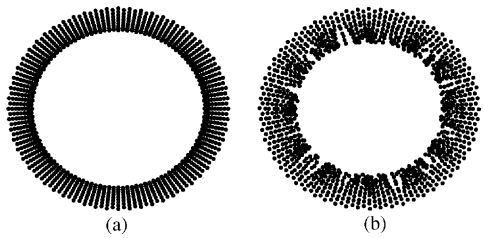

Fig. 18. Deformed rubber ring by stress points (at $t = 0.12$ ms): (a) Lagrangian kernel and (b) Eulerian kernel.

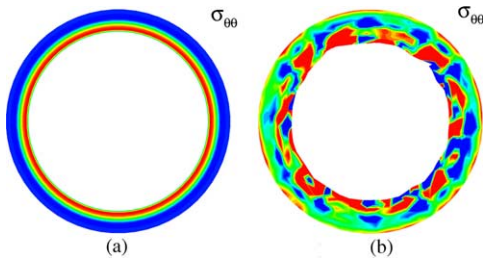

Fig. 19. $\sigma_{\theta\theta}$ distribution at $t = 0.12$ ms: (a) Lagrangian kernel and (b) Eulerian kernel.

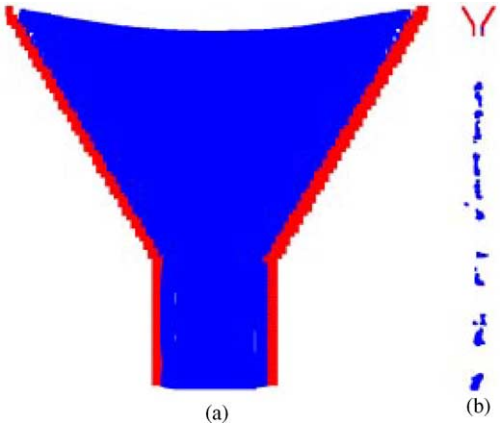

Fig. 20. Fluid flow in a funnel using an Eulerian kernel, (a) at the beginning of the computation, (b) at the end of the computation; the model sizes are rescaled to fit.

$$p = B\left(\left(\frac{\varrho}{\varrho_0}\right)^{\gamma} - 1\right). \tag{77}$$

The initial density ϱ_0 for water is 0.001 g/mm^3, the exponent $\gamma = 7$ and $B = 0.4704$ MPa. Fig. 20 shows the flow out of the funnel for an Eulerian kernel. With a Lagrangian kernel the simulation becomes unstable. The velocities explode suddenly, so that the flow cannot even be drawn after the instability.

10. Conclusions

A meshfree particle method based on Krongrauz and Belytschko [27] has been developed and tested. In this method, the trial functions are corrected derivatives of the kernel functions and the test functions are Shepard functions. Quadrature of the Galerkin weak form was performed over the particles and a set of slave particles, often called stress points. It was shown that this method is substantially more robust for solid mechanics problems than SPH and that it is able to deal with unstable phenomena such as shear bands and fracture. The rate of convergence of the approximation is close to two in the displacement norm; two is the optimal rate for an approximation with linear completeness.

We have also reviewed the original symmetrized SPH method, the Randles–Libersky normalization, and MLS-based methods such as EFG and compared the results of EFG–KBM with these other methods. In making these comparisons, we have considered both problems that have closed-form solutions, some where only experimental results are available, and some where only qualitative evaluations can be made.

A noteworthy result, which was also reported in Belytschko et al. [2] for a nonsymmetrized version of SPH, is that for a beam problem, symmetrized SPH solutions do not converge when the domain of influence (smoothing length) is decreased at the same rate as the particle spacing. The method is convergent when the domain of influence is kept constant in size. However, constant domains of influence are not suitable for practical computations since the sparsity of the discrete equations is severely diminished.

We also showed that EFG–KBM is capable of treating natural boundary conditions, such as traction free boundaries without any explicit enforcement of these conditions. This was demonstrated in a problem of plane wave reflection; Randles and Libersky [41] have argued that a similar correction that they called a normalization requires explicit treatment of the traction boundary conditions.

It is interesting to note that the best results were obtained for the EFG method with cell integration. However, this method is significantly more expensive than SPH or stress point methods, and our results

indicate that its accuracy per computation time is inferior to EFG–KBM. The SPH and Randles–Libersky methods are more dispersive than the other methods, which results in a higher error in the L_2 velocity norm, but the peak as well as the wave velocity are matched quite well.

This new particle method, EFG–KBM, was applied to failure problems involving concrete and metals and its performance was compared to some of the other particle methods reviewed here, such as SPH. Concerning the kernel, it can be said that the Lagrangian kernel seems to be more effective for solids than Eulerian kernels. For a metal plate under compressive loading with viscoplastic material behavior, it was shown that the Lagrangian kernel yielded stable solutions in the tensile regime while for the Eulerian kernel large oscillation could be observed. Similarly, for a hyperelastic ring, the Eulerian kernel exhibited a distinct instability. These instabilities confirm the analysis by Xiao et al. [47] that showed that Eulerian kernels distort the domain (in stress space) of material stability. However, several cases were reported, such as the formation of shear bands in the metallic ring, where Eulerian kernels performed quite well even in tension.

The influence of the Lagrangian and Eulerian kernel with respect to the computational effort cannot be answered definitively. The advantage of the Lagrangian kernel is that a time consuming neighbor search and the calculation of the shape functions needs to be done only once at the beginning of the calculation. However, whereas Eulerian kernels naturally handle contact, Lagrangian kernels require contact algorithms. However, the more pertinent issue is the relative capability of Eulerian and Lagrangian kernels to handle large deformations. Lagrangian kernels cannot handle very large deformations, such as found in fluids, at least not without some kind of reinitialization of the domains of influence. However, for the simulations of the failure of solids, Lagrangian kernels appear to be more robust and they are easily able to handle the magnitude of deformations encountered in this class of problems. Therefore, in fluid structure interaction problems, it is probably preferable to model the solid with Lagrangian kernels and the fluid with Eulerian kernels.

Acknowledgements

The support of Office of the Naval Research and the Army Research Office is gratefully acknowledged.

References

[1] S. Beissel, T. Belytschko, Nodal integration on the element-free Galerkin method, Comput. Methods Appl. Mech. Engrg. 139 (1996) 49–74.
[2] T. Belytschko, Y. Krongauz, J. Dolbow, C. Gerlach, On the completeness of meshfree particle methods, Int. J. Numer. Methods Engrg. 43 (1998) 785–819.
[3] T. Belytschko, M. Fleming, D. Organ, Y. Krongauz, W.K. Liu, Smoothing and accelerated computations in the element free Galerkin method, J. Comput. Appl. Math. 74 (1996) 111–126.
[4] T. Belytschko, Y. Krongauz, D. Organ, P. Krysl, Meshless methods: An overview and recent developments, Comput. Methods Appl. Mech. Engrg. 139 (1996) S.3–S.47.
[5] T. Belytschko, Y.Y. Lu, L. Gu, Element-free Galerkin methods, Int. J. Numer. Methods Engrg. 37 (1994) 229–256.
[6] T. Belytschko, Y. Guo, W.K. Liu, S.P. Xiao, A unified stability analysis of meshless particle methods, Int. J. Numer. Methods Engrg. 48 (2000) 1359–1400.
[7] T. Belytschko, S.P. Xiao, Stability analysis of particle methods with corrected derivatives, Comput. Math. Appl. 43 (2000) 329–350.
[8] T. Belytschko, Crack propagation by element free Galerkin methods, Engrg. Fract. Mech. 51/2 (1995) 295–315.
[9] T. Belytschko, Y.Y. Lu, Element-free Galerkin methods for static and dynamic fracture, Int. J. Solids Strucut. 32 (1995) 2547–2570.
[10] T. Belytschko, W.K. Liu, B. Moran, Nonlinear Finite Elements for Continua and Structures, John Wiley and Sons, Ltd, New York, 2000.
[11] T. Belytschko, H.Y. Chiang, E. Plaskacz, High resolution two-dimensional shear band computations imperfections and mesh dependency, Comput. Methods Appl. Mech. Engrg. 119 (1994) 1–15.

[12] T. Black, T. Belytschko, Convergence of corrected derivative methods for second-order linear partial differential equations, Int. J. Numer. Methods Engrg. 44 (2) (1999) 177–203.
[13] J. Bonet, T.-S.L. Lok, Variational and momentum preservation aspects of Smooth Particle Hydrodynamics formulations, Comput. Methods Appl. Mech. Engrg. 180 (1999) 97–155.
[14] J.S. Chen, C.T. Wu, S. Yoon, Y. You, A stabilized conforming nodal integration for Galerkin meshfree-methods, Int. J. Numer. Methods Engrg. 50 (2001) 435–466.
[15] G.A. Dilts, Moving least squares particle hydrodynamics II: Conservation and boundaries, Int. J. Numer. Methods Engrg. (2000) 1503–1524.
[16] G.A. Dilts, Moving-least-squares-particle hydrodynamics I: Consistency and stability, Int. J. Numer. Methods Engrg. 44 (1999) S.1115–S.1155.
[17] G.A. Dilts, Some recent developments for moving-least-squares particle methods, First M.I.T. Conference on Computational Fluid and Soil Mechanics, June 12–14, 2001, Preprint, Massachusetts Institute of Technology, Cambridge, MA 02139, USA.
[18] C.T. Dyka, R.P. Ingel, An approach for tensile instability in smoothed particle hydrodynamics, Comput. Struct. 57 (1995) 573–580.
[19] C.T. Dyka, R.P. Ingel, Addressing Tension Instability in SPH Method, Naval Research Laboratory, Washington, 1994.
[20] R.A. Gingold, J.J. Monaghan, Smoothed particle hydrodynamics: theory and applications to non-spherical stars, Mon. Not. R. Astr. Soc. 181 (1977) 375–389.
[21] K. Girkmann, Flaechentragwerke, 6, Springer Verlag, Wiley, New York, 1974.
[22] D.E. Grady, D.A. Benson, Fragmentation of metal rings by electromagnetic loading, Exp. Mech. 12 (187) (1983) 393–400.
[23] S. Hao, W.K. Liu, C.T. Chang, Computer implementation of damage models by finite element and meshfree methods, Comput. Methods Appl. Mech. Engrg. 187 (2000) 401–440.
[24] G.R. Johnson, S.R. Beissel, Normalized smoothing functions for SPH impact computations, Int. J. Numer. Methods Engrg. 39 (1996) S.2725–S.2741.
[25] L.M. Kachanov, Time of the rupture process under creep conditions, Izv. Akad. Nauk SSR Otd. Tech. 8 (1958) 26–31.
[26] L.M. Kachanov, Foundations of the Theory of Plasticity, North Holland, London, 1971.
[27] Y. Krongauz, T. Belytschko, Consistent pseudo derivatives in meshless methods, Comput. Methods Appl. Mech. Engrg. 146 (1997) 371–386.
[28] L.D. Libersky, A.G. Petschek, Smooth particle hydrodynamics with strength of materials, Advances in the Free Lagrange Method, Lecture Notes in Physics, 395, 1990.
[29] W.K. Liu, S. Jun, J. Adee, T. Belytschko, Reproducing kernel particle method for structural dynamics, Int. J. Numer. Methods Engrg. 38 (1995) 1665–1679.
[30] W.K. Liu, S. Jun, Y.F. Zhang, Reproducing kernel particle methods, Int. J. Numer. Methods Fluid 20 (1995) 1081–1106.
[31] Y.Y. Lu, T. Belytschko, L. Gu, A new implementation of the element free Galerkin method, Comput. Methods Appl. Mech. Engrg. 113 (1994) 397–414.
[32] L.B. Lucy, A numerical approach to the testing of fission hypothesis, Astronom. J. 82 (1977) 1013–1024.
[33] J.J. Monaghan, Kernel estimates as a basis for general particle methods in hydrodynamics, J. Comput. Phys. 46 (1982) S.429–S.453.
[34] J.J. Monoghan, An introduction to sph, Comput. Phys., Commun. 48 (1988) 89–96.
[35] N.F. Mott, Fragmentation of shell cases, Proc. Roy. Soc. London 300 (1947) 300–308.
[36] B. Nayroles, G. Touzot, P. Villon, Generalizing the finite element method: diffuse approximation and diffuse elements, Comput. Mech. 10 (1992) 307–318.
[37] A. Needleman, Dynamic shear band development in plane strain, J. Appl. Mech. 56/1 (March) (1989).
[38] P.E. Petersson, Crack growth development of fracture zone in plain concrete and similar materials, Report No. TVBM-1006, Division of Building Materials, 1981, University of Lund, Sweden 1981.
[39] T. Rabczuk, Numerische Untersuchungen zum Fragmentierungsverhalten von Beton mit Hilfe der SPH-Methode, Dissertation, Inst. Massivbau, Universitaet Karlsruhe, 2002.
[40] T. Rabczuk, J. Eibl, Simulation of high velocity concrete fragmentation using SPH/MLSPH, Int. J. Numer. Methods Engrg. 56 (2003) 1421–1444.
[41] P.W. Randles, L.D. Libersky, Recent improvements in SPH modeling of hypervelocity impact, Int. J. Impact Engrg. 20 (1997) 525–532.
[42] P.W. Randles, L.D. Libersky, Normalized SPH with stress points, Int. J. Numer. Methods Engrg. 48 (2000) 1445–1462.
[43] Schmidt-Hurtienne: Ein dreiaxiales Schaedigungsmodell zur Beschreibung des Dehnrateneffektes von Beton, Dissertation, Institut fuer Massivbau und Baustofftechnologie, Universitaet Karlsruhe, 2000.
[44] J.C. Simo, T.J.R. Hughes, On the variational foundations of assumed strain methods, J. Appl. Mech. 53 (1986) 1685–1695.
[45] J.W. Swegle, S.W. Attaway, M.W. Heinstein, F.J. Mello, Hicks D.L., An Analysis of Smoothed Particle Hydrodynamics, Sandia Report SAND93-2513,1994,SNL,Albuquerque, NM 87185.
[46] J.W. Swegle, D.A. Hicks, Smooth particle hydrodynamics stability analysis, J. Comput. Phys. 116 (1995) 123–134.
[47] S.P. Xiao, T. Belytschko, Material stability analysis of particle methods, Adv. Comput. Math., accepted for publication.